Chemical abundances in Seyfert galaxies – X. Sulphur abundance estimates

Oli L. Dors[1]⋆, M. Valerdi[2]†, R. A. Riffel[3], R. Riffel[4], M. V. Cardaci[5,6], G. F. Hägele[5,6], Mark Armah[4],
M. Revalski[7], S. R. Flury[8], P. Freitas-Lemes[1], E. B. Amôres[9], A. C. Krabbe[1], L. Binette[10], A. Feltre[12],
T. Storchi-Bergmann[4]

[1] *Universidade do Vale do Paraíba, Av. Shishima Hifumi, 2911, Cep 12244-000, São José dos Campos, SP, Brazil*
[2] *Instituto Nacional de Astrofísica, Óptica y Electrónica (INAOE), Luis E. Erro No. 1, Sta. Ma. Tonantzintla, Puebla, C.P. 72840, México.*
[3] *Departamento de Física, Centro de Ciências Naturais e Exatas, Universidade Federal de Santa Maria, 97105-900, Santa Maria, RS, Brazil*
[4] *Departamento de Astronomia, Universidade Federal do Rio Grande do Sul, Av. Bento Gonçalves 9500, Porto Alegre, RS, Brazil*
[5] *Facultad de Ciencias Astronómicas y Geofísicas, Universidad Nacional de La Plata, Paseo del Bosque s/n, 1900 La Plata, Argentina.*
[6] *Instituto de Astrofísica de La Plata (CONICET-UNLP), La Plata, Avenida Centenario (Paseo del Bosque) S/N, B1900FWA, Argentina*
[7] *Space Telescope Science Institute, 3700 San Martin Drive, Baltimore, MD 21218, USA*
[8] *Department of Astronomy, University of Massachusetts Amherst, Amherst, MA 01002, USA*
[9] *Departamento de Física, Universidade Estadual de Feira de Santana, Av. Transnordestina, S/N, CEP 44036-900 Feira de Santana, BA, Brazil*
[10] *Instituto de Astronomía, Universidad Nacional Autónoma de México, A.P. 70-264, 04510 México, D.F., México, México*
[11] *Département de physique, de génie physique et d'optique, Université Laval, Québec, QC G1V 0A6, Canada*
[12] *Osservatorio di Astrofisica e Scienza dello Spazio di Bologna, Via P. Gobetti 93/3, 40129 Bologna, Italy*

ABSTRACT

For the first time, the sulphur abundance relative to hydrogen (S/H) in the Narrow Line Regions of a sample of Seyfert 2 nuclei (Sy 2s) has been derived via direct estimation of the electron temperature. Narrow emission line intensities from the SDSS DR17 [in the wavelength range $3000 < \lambda(\text{Å}) < 9100$] and from the literature for a sample of 45 nearby ($z < 0.08$) Sy 2s were considered. Our direct estimates indicate that Sy 2s have similar temperatures in the gas region where most of the S^+ ions are located in comparison with that of star-forming regions (SFs). However, Sy 2s present higher temperature values ($\sim 10\,000$ K) in the region where most of the S^{2+} ions are located relative to that of SFs. We derive the total sulphur abundance in the range of $6.2 \lesssim 12 + \log(\text{S/H}) \lesssim 7.5$, corresponding to 0.1 - 1.8 times the solar value. These sulphur abundance values are lower by ~ 0.4 dex than those derived in SFs with similar metallicity, indicating a distinct chemical enrichment of the ISM for these object classes. The S/O values for our Sy 2 sample present an abrupt (~ 0.5 dex) decrease with increasing O/H for the high metallicity regime [$12 + \log(\text{O/H}) \gtrsim 8.7)$], what is not seen for the SFs. However, when our Sy 2 estimates are combined with those from a large sample of star-forming regions, we did not find any dependence between S/O and O/H.

Key words: galaxies: Seyfert – galaxies: active – galaxies: abundances –ISM: abundances –galaxies: evolution –galaxies: nuclei

1 INTRODUCTION

Sulphur is mainly produced via α-capture in the inner layers of massive stars (e.g. Woosley & Weaver 1995; Nomoto et al. 2013) and it is a truly non-refractory element in the interstellar medium (ISM). Due to these features, the sulphur abundance and its abundance relation with the oxygen (S/O) place constraints on stellar nucleosynthesis calculations, variations of the Initial Mass Function (IMF) of stars as well as in the analysis of the oxygen depletion onto dust grains (e.g. Garnett 1989; Savage & Sembach 1996; Henry et al. 2004).

Over time, several studies have obtained sulphur (and other α-elements) and oxygen abundances in star-forming regions (H II regions and H II galaxies, hereafter SFs; e.g. Pagel 1978; Shields & Searle 1978; Vilchez et al. 1988; Christensen et al. 1997; Garnett

et al. 1997; Vermeij & van der Hulst 2002; Kennicutt et al. 2003; Pérez-Montero et al. 2006; Hägele et al. 2008; López-Sánchez & Esteban 2009; Berg et al. 2013; Dors et al. 2016; Fernández et al. 2019; Arellano-Córdova et al. 2020; Berg et al. 2020; Rogers et al. 2021). However, the S/O versus O/H relation is still ill-defined. In fact, some authors (e.g. Vilchez et al. 1988; Díaz et al. 1991; Dors et al. 2016; Díaz & Zamora 2022) have found evidence that S/O decreases as O/H increases. On the other hand, constant S/O abundance over a wide range of O/H (a gas phase metallicity tracer[1]) is supported by a growing body of studies (e.g. Garnett 1989; Kennicutt et al. 2003; Izotov et al. 2006; Guseva et al. 2011; Berg et al. 2020; Rogers et al. 2021).

Abundance estimates in stellar atmospheres, derived from absorption features, have confirmed the above contradictory results and

---

⋆ E-mail: olidors@univap.br
† E-mail: mabel.astro@gmail.com

[1] For a review see Maiolino & Mannucci (2019) and Kewley et al. (2019).

several scenarios have been reported: (*i*) a constant increase of the S/Fe abundance ratio as metallicity[2] decreases (e.g., Israelian & Rebolo 2001; Takada-Hidai et al. 2002), (*ii*) an increase of S/Fe followed by a constant value at the metal-poor regime as metallicity decreases (Nissen et al. 2004, 2007) and (*iii*) a bimodal behaviour of S/Fe at the metal-poor regime (Caffau et al. 2005). However, recent chemical abundance determinations in stellar atmospheres have found a decrease of S/Fe with increasing Fe/H (Costa Silva et al. 2020; Lucertini et al. 2022). Interestingly, abundance estimates based on absorption lines in damped Lyα (DLA) systems (Centurión et al. 2000) showed a decrease of S/Zn with the increase of Zn/H (a metallicity tracer, Pettini et al. 1997), indicating that α-element burning happens at different times for different elements in massive stars (see also Bonifacio et al. 2001; Prochaska & Wolfe 2002; Fathivavsari et al. 2013; Fox et al. 2014). However, gas-phase abundances in DLAs must be corrected for dust depletion effects, producing additional difficulties in the interpretation of abundance ratio trends (e.g. Roman-Duval et al. 2022).

Sulphur and oxygen abundances have also been largely derived for Planetary Nebulae (PNe, e.g. Barker 1980; Aller & Czyzak 1983; Costa et al. 2004; Bernard-Salas et al. 2008; Cavichia et al. 2017; Pagomenos et al. 2018; Walsh et al. 2018; Espíritu & Peimbert 2021; García-Rojas et al. 2022). In particular, Fang et al. (2018), who combined S and O abundances, obtained a clear decrease of S/O with O/H for 10 PNe in the Andromeda Galaxy (M 31) with estimates relying on data from the literature. Additionally, these authors found that their sample of PNe have abundance estimates ∼0.2–0.4 dex lower than the expected sulphur -to-oxygen abundance solar value assuming log(S/O)$_{\odot}$ = −1.43 (Grevesse & Sauval 1998; Allende Prieto et al. 2001). This discrepancy has previously been attributed to the inadequacy of the Ionization Correction Factors (ICFs) used to correct the presence of unobserved sulphur ions (the so-called "sulphur anomaly") by Henry et al. (2004) and Milingo et al. (2010). However, the PN abundance estimates by Fang et al. (2018) are in agreement with those derived in H II regions also located at the Andromeda Galaxy by Zurita & Bresolin (2012), confirming their results. Moreover, Delgado-Inglada et al. (2014), who computed a large grid of photoionization models that covers a wide range of physical parameters and is representative of most observed PNe, proposed a robust ICF for the sulphur and, by using optical observational data for a large sample, confirmed that S/O decreases with O/H. However, it is worth to mention that, contrary to presently accepted thinking, Jenkins (2009) showed that sulphur can deplete by up to ∼1 dex, which might account for some of the decrease observed.

Contrary to SFs, stars, DLA systems and PNe, the sulphur abundance is poorly known in Active Galactic Nuclei (AGNs) or only qualitative estimates are available in the literature. The first (qualitative) sulphur estimates for this class of objects seems to have been performed by Storchi-Bergmann & Pastoriza (1990), who compared the intensity of the [N II]($\lambda\lambda$6548, 6584)/Hα and [S II]($\lambda\lambda$6716, 31)/Hα line ratios predicted by photoionization models with observational data from a sample of 177 Seyfert 2 galaxies. These authors found that models assuming sulphur abundances ranging from half to five times the solar abundance reproduce the observational data. These estimates can be somewhat uncertain because the model fittings by Storchi-Bergmann & Pastoriza (1990) do not consider the lines emitted by S^{2+}, which can be the most abundant sulphur ion

and occurs as a result of high ionization degree of the AGNs (e.g. Richardson et al. 2014; Pérez-Díaz et al. 2021).

Recently, Dors et al. (2020b) proposed a new methodology for the T_e-method – a conventional and reliable method (Pilyugin 2003; Toribio San Cipriano et al. 2017) based on direct estimates of the electron temperature (for a review see Peimbert et al. 2017; Pérez-Montero 2017) – which makes it possible to estimate the O/H abundance in Seyfert 2 nuclei (hereafter Sy 2s). Further studies based on this methodology, for the first time, permitted direct abundance estimates of the argon (Monteiro & Dors 2021), neon (Armah et al. 2021) and helium (Dors et al. 2022) in the narrow line regions (NLRs) of a large sample of Sy 2s. Generally, this class of AGN presents solar or oversolar metallicities (12 + log(O/H) ≳ 8.7, e.g. Shields & Searle 1978; Groves et al. 2006; Dors et al. 2020a) and gas with high ionization. These features make it possible to measure some auroral lines (e.g. [O III]λ4363, [N II]λ5755) in the high metallicity regime, which are difficult to detect in SFs (e.g. van Zee et al. 1998; Díaz et al. 2007; Dors et al. 2008). However, it is worthwhile to point out some difficulties in applying the T_e-method to derive abundances in AGNs, for instance: (i) due to the large width of Hγ, in several cases, this Balmer line is blended with the temperature-sensitive auroral line [O III]λ4363 in AGN spectra; (ii) although AGNs have a high ionization degree, its high metallicity (e.g. Groves et al. 2006) produces measurements of [O III]λ4363 with low signal/noise ratio, which translates into a large abundance uncertainty (e.g. Dors et al. 2022) and (iii) temperature estimates from distinct gas regions in AGNs are barely found in the literature, making it difficult to carry out any statistical study. In any case, with the current observational data and methodologies available in the literature it is possible to obtain (relatively) precise sulphur and oxygen abundances, producing important constraints to the studies of stellar nucleosynthesis in the high metallicity regime. In fact, even the recent stellar nucleosynthesis models (e.g. Ritter et al. 2018) do not consider oversolar metallicities despite metallicity has an impact on the stellar product (e.g. Gronow et al. 2021).

Taking advantage of the availability of spectroscopic data of Sy 2s in the literature, data provided by the Sloan Digital Sky Survey (York et al. 2000) and motivated by the new methodology proposed by Dors et al. (2020b), in this work, the last in a series of ten papers, we present direct S and O abundance estimates for the NLRs of a sample of 45 Sy 2s. This study is organized as follows. In Section 2 the observational data is presented. The methodology used to estimate the sulphur and oxygen abundances is presented in Sect. 3. The results and discussion are given in Sect. 4. Finally, the key findings are summarised in Sect. 5.

2 OBSERVATIONAL DATA

In order to obtain a sample of Sy 2s with observational intensities of narrow (Full Width Half Maximum < 1000 km s^{-1}) optical emission lines, we used spectroscopic data made available through the Sloan Digital Sky Survey Data Release 17[3], SDSS DR17 (Abdurro'uf et al. 2022). In the present study, the procedures for selection of Sy 2s, emission line measurements, reddening correction and the stellar population continuum subtraction were the same as described by Dors et al. (2022), therefore, we summarized these processes below.

For each spectrum downloaded from the SDSS DR17, we performed the extinction correction using the Cardelli et al. (1989)

---

[2] The metallicity in stars is usually traced by Fe/H abundance ratio (e.g., Allende Prieto et al. 2004).

[3] SDSS DR17 spectroscopic data are available at `https://dr17.sdss.org/optical/plate/search`

emission line intensities (in relation to Hβ=1.0) and the literature references from which the data were compiled are listed. In this Table, the theoretical relation $I(\lambda 9069) = 0.40 \times I(\lambda 9532)$ between the [S III] emission-lines is assumed.

In Fig. 2, a log([O III]λ5007/Hβ) vs. log([N II]λ6584/Hβ) diagnostic diagram, the observational data and the above criteria (Equations 1 and 2) are shown. It can be seen that the Sy 2 sample covers a large range of ionization degree and metallicity, since a wide range of [O III]/Hβ and [N II]/Hα line ratio intensities are seen (e.g. Groves et al. 2006; Feltre et al. 2016; Carvalho et al. 2020).

The observational data sample is heterogeneous, in the sense that the spectra were obtained with distinct instrumentation (e.g. long-slit, fiber spectroscopy), aperture, reddening correction procedures, etc. These features could produce artificial scattering or biases in the derived abundances. Dors et al. (2020a, 2021) and Armah et al. (2021) presented a complete discussion on the use of a heterogeneous sample and its possible implications on abundance estimates. These authors pointed out that the effects of considering such a heterogeneous sample on abundance estimates produce uncertainties of ~ 0.1 dex, i.e. in the same order or even lower than those derived by applying the T_e-method (e.g. Kennicutt et al. 2003; Hägele et al. 2008) and strong-line methods (e.g. Storchi-Bergmann et al. 1998; Denicoló et al. 2002). Moreover, Kewley et al. (2005) presented a detailed analysis of the effect of considering different apertures on the determinations of physical parameters of galaxies. These authors found that for aperture capturing less than 20 per cent of the total galaxy emission, the derived metallicity can differ by a factor of about 0.14 dex from the value obtained when the total galaxy emission is considered. However, only abundances of the nuclear regions are being considered here; therefore, the aperture effect on our estimates is not significant. Additional analysis of uncertainties in abundance estimates derived from distinct instrumentation and/or aperture has been addressed, for instance, by Mannucci et al. (2021), who analysed the Diffuse Ionized Gas (DIG) contribution to the nebular emission of SFs. These authors, specifically, found that the [S II] line fluxes tend to be more affected in comparison with other optical line fluxes. Mannucci et al. (2021) also found that when spectra of local H II regions are extracted using large enough apertures while still avoiding the DIG, the observed line ratios are the same as in more distant galaxies. Therefore, there should not be any bias in our sample as a result of the usage of different instruments (see also Arellano-Córdova et al. 2022; Pilyugin et al. 2022). However, the requirement for the presence of the weak [O III]λ4363 line (about 100 times weaker than Hβ) in the SDSS spectra yields a bias in our analysis, in the sense that objects with very high metallicity, where the gas suffers strong cooling and the electron temperature is low enough not to produce significant emission of this line, are mostly excluded. In fact, for instance, Dors et al. (2020a) selected from the SDSS DR7 database (Abazajian et al. 2009), 463 confirmed Sy2 spectra with only 150 objects having [O III]λ4363 measured with (S/N) > 2 and from these, only 36/150 have oversolar metallicity according to the T_e-method applied by Dors et al. (2020b). Thus, abundance determinations obtained in the present study do not extend to objects with the highest expected metallicity (see also van Zee et al. 1998; Izotov et al. 2006; Flury & Moran 2020).

Another issue is the SF emission contribution to our AGN spectra, which can have a greater impact on the observed line fluxes for the most distant objects. Davies et al. (2014) presented a spatially resolved study of the active galaxy NGC 7130 ($z = 0.016$) and found that SFs are responsible for 30 and 65 per cent of the [O III] and Hα luminosity, respectively. Moreover, Vidal-García et al. (2022) compared results from the NLR photoionization models (Feltre et al.

2016) incorporated into the BEAGLE (Bayesian SED-fitting, Chevallard & Charlot 2016) code with observational spectroscopic data and showed that the SF Hβ flux contribution to the total nuclear flux of an active galaxy can range from 0 to 50 per cent. However, we emphasize that, in principle, the SF flux contribution has a minimal effect on AGN abundance estimates when a sample of objects is considered. This assertion is supported by Thomas et al. (2019), who demonstrated that the aperture effect (and consequently SF contribution) has a negligible impact on metallicity estimates once comparable mass-metallicity relations for galaxies in four redshift bins were considered.

Since the [S III] lines of Seyfert galaxies are rarely found in the literature due to the fact that they are located in the near infrared which there are few instruments operating, it is worthwhile to compare their emission line flux ratios with those of SFs. In this regard, we consider emission line intensities of H II galaxies (44 objects) and Giant H II regions (GHRs, 34 objects) presented by Hägele et al. (2006, 2008, 2011, 2012). Besides, we compare the Sy 2 emission lines considered in this work with those from 378 disk H II regions located in 6 local spiral galaxies, which have been made available by the CHAOS project[4], and presented by Berg et al. (2015, 2020), Croxall et al. (2015, 2016), and Rogers et al. (2021, 2022). This comparison (see also Díaz & Zamora 2022) is shown in Fig. 3. A clear correlation is derived between the two dataset since both line ratios are dependent on the ionization degree of the gas. Interestingly, Sy 2 nuclei present similar [S III]/[S II] line ratio intensities to those of SFs. The Sy 2 [O III]/[O II] line ratio intensities are in consonance with those of H II galaxies and GHRs and are higher than those from disk H II regions.

3 ABUNDANCE ESTIMATES

For the Sy 2 sample previously described, we determined the sulphur and oxygen abundances relative to hydrogen. To do that, electron temperatures representing the zones where distinct ions are located in the gas phase, electron density and ionic abundances were calculated using the 1.1.13 version of PyNeb code (Luridiana et al. 2015), which permits an interactive procedure in the derivation of these parameters. The references for the predefined atomic parameters incorporated into the PyNeb code are listed in Table 1.

As the line measurements for some objects (9/45) of our sample does not present observational errors, the abundance uncertainties were estimated using Monte Carlo simulations. For each diagnostic line, we generate 1000 random values assuming a Gaussian distribution with a standard deviation equal to the associated uncertainty of 10 % and 20 % for strong (e.g. [O III]λ5007) and auroral (e.g. [O III]λ4363) line intensities involved in the diagnostics, respectively. Thereafter, an empirical Ionization Correction Factor (ICF) was considered in the derivation of the total sulphur abundance. For objects that have measured emission-line errors (36/45), the uncertainties in the final abundance values were obtained propagating the errors in the line measurements, electron temperature and electron density. Subsequently, the description of the employed methodology is presented.

3.1 Temperature estimations

Several studies have been directed to estimate the chemical composition of SFs and, in almost all of these estimates, it has been a common

---

[4] https://www.danielleaberg.com/chaos

Table 1. Atomic dataset used for collisionally excited lines of selected element ions.

Ion	Transition probabilities	Collisional strengths
S^+	Froese Fischer et al. (2006)	Tayal & Zatsarinny (2010)
S^{2+}	Froese Fischer et al. (2006)	Tayal & Gupta (1999)
O^+	Wiese et al. (1996)	Kisielius et al. (2009)
O^{2+}	Froese Fischer & Tachiev (2004), Storey & Zeippen (2000)	Storey et al. (2014)

Table 2. Estimates of $T_e(O^{2+})$, $T_e(N^+)$ and $T_e(S^{2+})$ used to obtain the relations given by Eqs. 3 and 4. The line ratios are: $RO3 = ([O\,\textsc{iii}]\lambda4959+\lambda5007)/\lambda4363$, $RN2 = ([N\,\textsc{ii}]\lambda6548+\lambda6584)/\lambda5755$, $RS3 = ([S\,\textsc{iii}]\lambda9069+\lambda9532)/\lambda6312$ and $RS2 = [S\,\textsc{ii}]\lambda6716/\lambda6731$.

Object	$RO3$	$RN2$	$RS3$	$RS2$	$T_e(O^{2+})$[K]	$T_e(N^+)$[K]	$T_e(S^{2+})$[K]	N_e[cm^{-3}]	Ref.
IZw 92	42.62 ± 8.52	66.50 ± 13.30	—	0.92 ± 0.09	16350 ± 1646	9929 ± 788	—	1176 ± 427	1
Mrk 3	69.41 ± 13.88	87.29 ± 17.45	—	0.89 ± 0.08	13151 ± 1059	8969 ± 638	—	1221 ± 395	2
Mrk 78	112.90 ± 22.58	95.31 ± 19.06	—	1.11 ± 0.11	11023 ± 743	8754 ± 607	—	467 ± 229	2
Mrk 34	100.90 ± 20.18	87.27 ± 17.45	—	1.02 ± 0.10	11445 ± 800	9012 ± 643	—	691 ± 280	2
Mrk 1	69.09 ± 13.81	135.45 ± 27.09	—	0.94 ± 0.09	13187 ± 1060	7773 ± 481	—	1000 ± 362	2
Mrk 533	95.00 ± 19.00	240.00 ± 48.00	—	0.86 ± 0.08	11681 ± 834	6591 ± 346	—	1319 ± 429	3
Mrk 612	60.00 ± 12.00	112.00 ± 22.40	—	1.36 ± 0.13	13993 ± 1199	8304 ± 551	—	87 :	3
ESO 138 G1	34.23 ± 6.84	47.73 ± 9.54	—	0.97 ± 0.09	18386 ± 2084	11457 ± 1055	—	1003 ± 366	4
NGC 2992	40.36 ± 8.07	98.20 ± 19.64	—	1.12 ± 0.11	16831 ± 1736	8659 ± 595	—	514 ± 266	5
NGC 2210	24.36 ± 4.87	117.77 ± 23.55	—	1.06 ± 0.10	22797 ± 3095	8143 ± 527	—	744 ± 328	5
NGC 5506	73.57 ± 14.70	168.50 ± 33.70	—	0.92 ± 0.09	12859 ± 1012	7279 ± 421	—	1074 ± 386	5
Mrk 348	23.7 ± 2.4	31.8 ± 11.9		0.83 ± 0.03	28600 ± 4700	21700 ± 6100	—	1940 ± 245	6
Mrk 607	29.7 ± 10.2	80.6 ± 16.2		0.87 ± 0.11	23500 ± 2700	10200 ± 1300	—	1548 ± 707	6
56067-0382	41.43 ± 8.29	12.29 ± 2.46	—	1.06 ± 0.16	16604 ± 1694	31367 ± 8555	—	669 ± 463	7
55539-0167	82.20 ± 16.44	24.49 ± 4.90	—	1.13 ± 0.17	12334 ± 928	16655 ± 2244	—	442 ± 349	7
56001-0293	109.00 ± 21.80	37.02 ± 7.40	—	1.39 ± 0.21	11159 ± 760	13147 ± 1393	—	58 :	7
55742-0383	99.80 ± 19.96	42.04 ± 8.41	—	1.13 ± 0.17	11497 ± 806	12245 ± 1202	—	432 ± 340	7
55302-0655	41.20 ± 8.24	47.71 ± 9.54	—	1.24 ± 0.19	16672 ± 1708	11537 ± 1068	—	266 ± 0	7
56568-0076	105.33 ± 21.07	96.13 ± 19.23	—	1.03 ± 0.15	11280 ± 780	8715 ± 604	—	660 ± 407	7
56566-0794	94.80 ± 18.96	127.06 ± 25.41	4.36 ± 0.87	1.18 ± 0.18	11713 ± 838	7968 ± 505	21665 ± 3991	342 :	7
55181-0154	130.33 ± 26.07	—	3.85 ± 0.77	0.98 ± 0.15	10508 ± 675	—	24380 ± 5015	786 ± 474	7
56088-0473	128.33 ± 25.67	—	18.00 ± 3.60	1.09 ± 0.16	10566 ± 682	—	9244 ± 747	502 ± 349	7
56034-0154	84.86 ± 16.97	—	12.00 ± 2.40	1.09 ± 0.16	12184 ± 909	—	11052 ± 1070	527 ± 370	7
56626-0636	102.00 ± 20.40	—	3.49 ± 0.70	1.08 ± 0.16	11409 ± 795	—	27079 ± 6116	537 ± 371	7
55651-0052	177.00 ± 35.40	—	5.37 ± 1.07	1.06 ± 0.16	9576 ± 560	—	18131 ± 2884	549 ± 368	7
56206-0454	74.11 ± 14.82	—	6.17 ± 1.23	1.23 ± 0.18	12842 ± 1010	—	16315 ± 2354	267 :	7
55860-0112	71.09 ± 14.22	—	3.39 ± 0.68	1.02 ± 0.15	13038 ± 1038	—	27975 ± 6506	724 ± 448	7
55710-0116	107.71 ± 21.54	—	12.29 ± 2.46	0.92 ± 0.14	11189 ± 764	—	10917 ± 1047	1018 ± 578	7
56366-0928	47.50 ± 9.50	—	3.14 ± 0.63	1.00 ± 0.15	15523 ± 1474	—	30648 ± 7717	834 ± 517	7
56328-0550	81.67 ± 16.33	—	7.48 ± 1.50	1.28 ± 0.19	12373 ± 934	—	14339 ± 1821	190 :	7
55617-0758	76.80 ± 15.36	—	3.45 ± 0.69	0.90 ± 0.13	12640 ± 978	—	27394 ± 6222	1156 ± 609	7
56003-0218	67.14 ± 13.43	—	5.89 ± 1.18	0.97 ± 0.14	13337 ± 1088	—	16867 ± 2531	889 ± 504	7
55505-0654	198.75 ± 39.75	—	12.00 ± 2.40	1.12 ± 0.17	9268 ± 524	—	11052 ± 1072	422 ± 319	7

References: (1) Kraemer et al. (1994), (2) Koski (1978), (3) Shuder & Osterbrock (1981), (4) Alloin et al. (1992), (5) Shuder (1980), (6), Riffel et al. (2021a), (7) SDSS sample.

practice to use temperature relations derived from photoionization models to infer the temperatures in the unobserved ionization zones (e.g. Stasińska 1990; Garnett 1992; Pérez-Montero & Díaz 2003; Izotov et al. 2006). However, when temperature relations predicted by photoionization models simulating SFs are compared with direct estimates relying on auroral lines, large deviations are found, reaching up to ~ 5000 K (e.g. Hägele et al. 2008; Berg et al. 2020; Arellano-Córdova & Rodríguez 2020). Despite the fact that temperature relations for AGNs are barely found in the literature (see Dors et al. 2020b; Armah et al. 2021; Monteiro & Dors 2021), it seems that similar disagreement is also derived for this class of object. In fact, Riffel et al. (2021a) compared the $T_e(N^+)$-$T_e(O^{2+})$ relation predicted by photoionization models, built using the CLOUDY code (Ferland et al. 2013), with values derived from observational auroral

emission lines for a sample of 12 local Seyfert nuclei. The model predictions reproduce the direct temperature observations for all objects, except for Mrk 348 for which the direct $T_e(N^+)$ value is ~10 000 K higher than the predicted one. This object is know to host ionized gas outflows (Freitas et al. 2018) and probably the higher observed temperatures are due to extra heating caused by shocks (see Dors et al. 2021), which is not accounted in the photoionization models considered by Riffel et al. (2021a). Obviously, additional comparison with a larger sample of objects combined with kinematic studies (e.g. Xu et al. 2021; Flury et al. 2022, in preparation) of objects where gas outflow is detected, is necessary to confirm this result.

Since comparisons between observational emission line intensities and the ones predicted by photoionization models indicate that the main ionization source of most NLR of Sy 2s is the radiation emitted
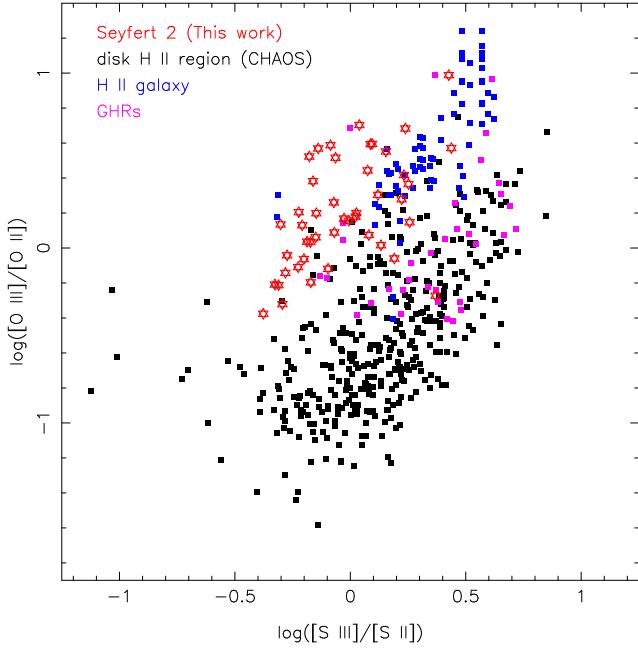
Figure 3. Logarithm of [O III]λ5007/[O II]λ3727 versus [S III]λ9069 + λ9532/[S II]λ6716+λ6731. Red points represent the Sy 2 sample (see Sect. 2) whose emission line intensities are listed in Table A1. Black points represent disk H II regions whose data were taken from the CHAOS project and obtained by Berg et al. (2015, 2020), Croxall et al. (2015, 2016) and Rogers et al. (2021, 2022). Blue points represent H II galaxies taken from Hägele et al. (2006, 2008, 2011, 2012) and pink points represent GHRs taken from Hägele et al. (2006).

by gas accretion into a supermassive black hole, for objects in the local universe (see e.g. Stasińska 1984; Ferland & Osterbrock 1986; Storchi-Bergmann et al. 1998; Groves et al. 2006; Feltre et al. 2016; Castro et al. 2017; Dors et al. 2017, 2020b; Pérez-Montero et al. 2019; Thomas et al. 2019; Carvalho et al. 2020; Armah et al. 2021) and also at high redshift (see e.g. Nagao et al. 2006; Matsuoka et al. 2009, 2018; Dors et al. 2014, 2018, 2019; Nakajima et al. 2018; Mignoli et al. 2019; Guo et al. 2020), we are able to apply the T_e-method to derive reliable estimates. However, the weak temperature-sensitive auroral emission-line measurements are barely available in the literature for AGNs, therefore we developed our own empirical method based on our sample.

To derive the empirical relations for our abundance estimates, we used auroral line intensities from our sample and those of Sy 2 NLRs available in the literature. Firstly, the observational intensities of the $RO3$=[O III](λ4959 + λ5007)/λ4363 and $RN2$=[N II](λ6548 + λ6584)/λ5755 line ratios were used to calculate T_e(O^{2+}) and T_e(N$^+$), respectively, for 18 objects, i.e. 7 objects of our sample (see Table A1) and 11 Sy 2 compiled by Dors et al. (2020b). To derive T_e(S^{2+}), we used the $RS3$=[S III](λ9069 + λ9532)/λ6312 line ratios for 14 objects (over 45) in our sample (see Table A1). For each object, the temperature estimates were performed assuming a constant electron density (N_e) value across the nebula, which is derived from the $RS2$=[S II]λ6716/λ6731 intensity ratio. In Table 2, the objects and their corresponding $RO3$, $RN2$, $RS3$ and $RS2$ line intensities ratios, the electron density, T_e(O^{2+}), T_e(N$^+$) and T_e(S^{2+}) temperature derived values are listed. We note that the object 56067-0382 has a T_e(N$^+$) higher than those derived for other objects and similar to the value derived for Mrk 348 by Riffel et al. (2021a). Probably 56067-0382 presents gas outflows but its temperatures were still

Table 3. Critical densities for collisional de-excitation for the lines involved in the present work. Values were calculated with the PyNeb code (Luridiana et al. 2015) assuming an electron temperature of 15 000 K.

Line	N_c (cm^{-3})
[O II]λ3726	4.72×10^3
[O II]λ3729	1.49×10^3
[O III]λ4363	2.88×10^7
[O III]λ5007	7.83×10^5
[N II]λ5755	1.87×10^7
[S III]λ6312	1.44×10^7
[N II]λ6484	1.04×10^5
[S II]λ6716	1.37×10^3
[S II]λ6731	3.67×10^3
[S III]λ9069	6.42×10^5

considered. Since in most cases only the [O III]λ4363 auroral line is measured (e.g. van Zee et al. 1998; Kennicutt et al. 2003), we proposed, as usual, temperature relations with respect to T_e(O^{2+}). In Fig. 4, T_e(N$^+$) and T_e(S^{2+}) are plotted against T_e(O^{2+}), with the values in units of 10^4 K. In the upper panel of this figure, the dashed line represents the equality between T_e(S^{2+}) and T_e(O^{2+}). As for SFs (e.g., see Hägele et al. 2008; Berg et al. 2020), clear correlations between the Sy 2 temperatures are observed, with a linear regression resulting in

$$t_e(\text{N}^+) = 0.36(\pm0.23) \times t_e(\text{O}^{2+}) + 0.55(\pm0.39), \qquad (3)$$

and

$$t_e(\text{S}^{2+}) = 2.23(\pm1.12) \times t_e(\text{O}^{2+}) - 0.74(\pm1.34), \qquad (4)$$

where $t_e = T_e/10^4$ K.

It can be seen in Fig. 4 that higher temperature values for S^{2+} are derived in comparison with those for O^{2+}, probably indicating that the former ion occupy an inner gas region than the latter. Conversely, an opposite result is derived for disk H II regions, i.e. T_e(O^{2+}) is $\sim$ 1000 K higher than T_e(S^{2+}) (e.g. Rogers et al. 2021). Hägele et al. (2006) analysed the relation between T_e(O^{2+}) and T_e(S^{2+}) using a sample that comprises H II galaxies, giant extragalactic H II regions, Galactic H II regions, and H II regions from the Magellanic Clouds (MCs). These authors found that the [S III] electron temperatures are higher than the corresponding [O III] estimations for most objects presenting temperatures higher than about 14 000K, mainly the metal poor H II galaxies, and the opposite behaviour for the coolest nebulae, mainly giant extragalactic H II regions, Galactic H II regions, and H II regions from the MCs, which present the highest metallicities. Taking into account the temperatures of the different samples studied by Hägele et al. (2008, H II galaxies that present the higher temperatures) and Rogers et al. (2021, galactic disk H II regions with lower temperatures), the T_e(S^{2+})-T_e(O^{2+}) behavior derived in the present paper for Sy 2s is the same as found by Hägele et al. (2006).

Spatially resolved observational studies of NLRs have found a profile of electron density along the AGN radius, in the sense that denser gas is located in the inner regions. For instance, Freitas et al. (2018), who obtained emission-line flux of two-dimensional maps from five bright nearby Seyfert nuclei, obtained electron densities ranging from $\sim$ 2500 cm^{-3} in the central parts to $\sim$ 100 cm^{-3} in the outskirts (see also Revalski et al. 2018a,b, 2021, 2022; Kakkad et al. 2018; Mingozzi et al. 2019; Ruschel-Dutra et al. 2021). Moreover, electron density estimations through the [Ar IV]λ4711/λ4740 line ratio, which traces the density in the innermost layers, showed values

of up to ~13 000 cm^{-3} (e.g. Congiu et al. 2017; Cerqueira-Campos et al. 2021). Thus, density values derived from [S ɪɪ] lines may not be representative of the region where S^{2+} ions are located, which could inherently introduce an error in the $T_e(S^{2+})$ values. In order to explore the influence of the electron density on the sulphur temperature estimations, we show in Fig. 5 the $t_e(S^{2+})$ derived assuming the N_e values from [S ɪɪ]$\lambda6716/\lambda6731$ line ratios (listed in Table 2) versus the estimations considering a fixed value of 13 000 cm^{-3}, as derived by Congiu et al. (2017) for the extended narrow-line region of the Seyfert 2 galaxy IC 5063. We notice a good agreement between the values, with a difference of $\sim 2\%$, which is lower than the uncertainty produced by the error in the line measurements ($\sim 10\%$, see Table 2). In Table 3 the critical density (N_c) values for the lines involved in the present work, calculated with the PɪNɪʙ code (Luridiana et al. 2015) assuming an electron temperature of 15 000 K, are listed. One can see that N_c values are higher than the electron density values (listed in Table A2) derived for our Sy 2 sample. Thus, electron density variations in NLRs have a minimal influence on our temperature estimates. For some objects, the emission-line errors are significant, thus frequently with density error bars larger than the determinations themselves. Therefore we use ":" to indicate that error bars are at least an order of magnitude larger than the expected density (see Table A2).

Due to the similarity among the S$^+$, N$^+$ and O$^+$ ionization potentials (23.33 eV, 29.60 eV and 35.12 eV, respectively) and because the [S ɪɪ]$\lambda\lambda4068, 4076$ and [O ɪɪ]$\lambda\lambda7320, 7330$ auroral lines are not measured in our sample of spectra, as in Rogers et al. (2021), we adopted $T_e(S^+)=T_e(O^+)=T_e(N^+)$. In objects for which it is possible to estimate directly $T_e(N^+)$ (7/45) and $T_e(S^{2+})$ (14/45), these temperatures were assumed as representative of the low and high ionization zones, respectively. Otherwise, when the [N ɪɪ]$\lambda5755$ and [S ɪɪɪ]$\lambda6312$ auroral emission-line measurements are not available, $T_e(N^+)$ and $T_e(S^{2+})$ were derived from the Eqs. 3 and 4, respectively. In Table A2, electron density and temperature values for the objects in our sample are presented.

3.2 Abundance derivation

For each object of our sample, using the emission line intensity ratios listed in Table A1, the electron temperature and electron density values (listed in Table A2) as well as the PɪNɪʙ code (Luridiana et al. 2015), we derived the sulphur (S$^+$, S^{2+}) and oxygen (O$^+$, O^{2+}) ionic abundances. Afterwards, applying an empirical ICF for the sulphur and a typical value for the oxygen ICF, the total abundances for the S/H and O/H were estimated. In what follows, we describe the methodology employed in the derivation of the abundance of each considered element.

3.2.1 Oxygen abundance

The total oxygen abundance in relation to the hydrogen one was derived assuming

$$\frac{O}{H} = ICF(O^+ + O^{2+}) \times \left[\frac{O^+}{H^+} + \frac{O^{2+}}{H^+}\right], \quad (5)$$

where ICF(O$^+$+O^{2+}) represents the Ionization Correction Factor for oxygen which takes into account the contribution of unobservable oxygen ions, whose emission lines are observed in other spectral bands such as X-rays (e.g. Cardaci et al. 2009, 2011; Bianchi et al. 2010; Bogdán et al. 2017; Maksym et al. 2019; Kraemer et al. 2020) and IR (e.g. Diamond-Stanic & Rieke 2012; Fernández-Ontiveros
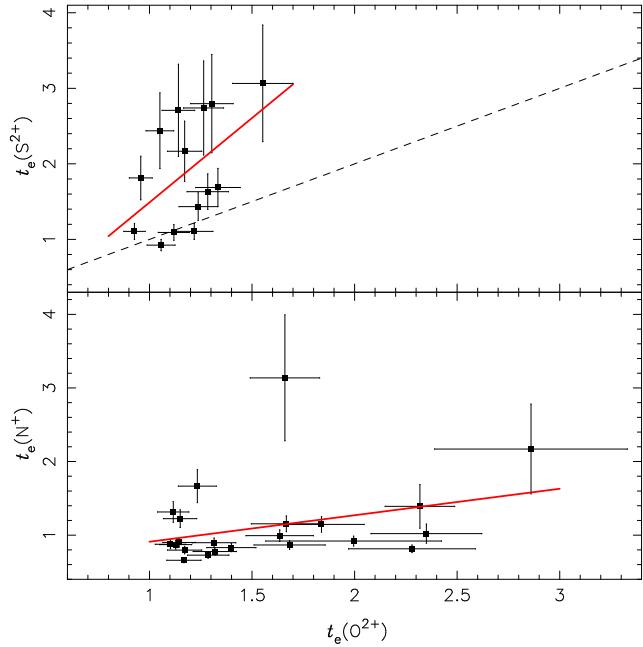
Figure 4. Comparing direct temperature values for different ions. Values are in units of 10^4 K. Botton panel: $t_e(O^{2+})$ and $t_e(N^+)$ are derived through the $RO3$=[O ɪɪɪ]$(\lambda4959+\lambda5007)/\lambda4363$ and $RN2$=[N ɪɪ]$(\lambda6548+\lambda6584)/\lambda5755$ line intensities ratios, respectively, and the electron density (from the $RS2$=[S ɪɪ]$\lambda6716/\lambda6731$) listed in Table 2, and by using version 1.1.13 of PɪNɪʙ code (Luridiana et al. 2015). The red line represents the linear regression to the points given by Eq. 3. Top panel: same as bottom panel but for $t_e(S^{2+})$ values derived from $RS3$=[S ɪɪɪ]$(\lambda9069 + \lambda9532)/\lambda6312$. Red line represents the linear regression to the points given by Eq. 4 while the dashed line the equality between the estimates.
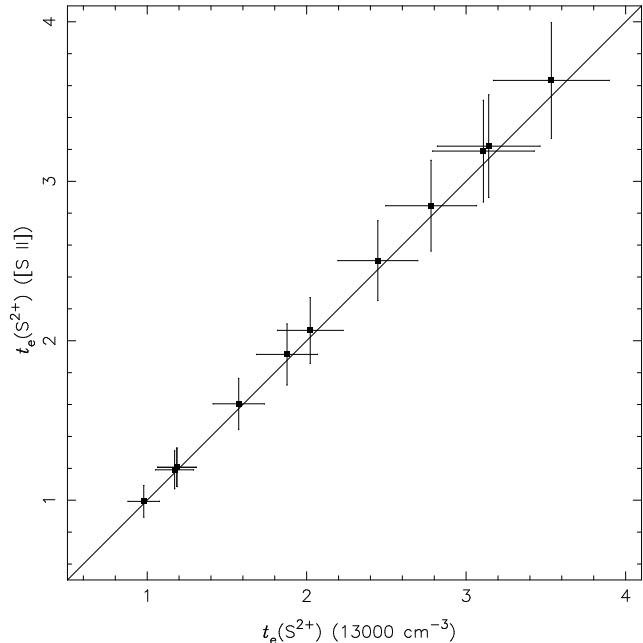
Figure 5. Comparison between electron temperatures (in units of 10^4 K) derived from the $RS3$=[S ɪɪɪ]$(\lambda9069 + \lambda9532)/\lambda6312$ assuming electron density estimations via the $RS2$=[S ɪɪ]$\lambda6716/\lambda6731$ (listed in Table 2) with the estimates assuming a value of 13 000 cm^{-3} as derived by Congiu et al. (2017) from [Ar ɪᴠ]$\lambda4711/\lambda4740$. Line represents the equality between the two estimates.

et al. 2016). The O^{2+}/H^+ ionic abundance was calculated by using the [O III]$\lambda 5007$/Hβ line ratio and assuming the direct $T_e(O^{2+})$ and N_e values derived from $RO3$ and $RS2$, respectively. The O^+/H^+ abundance was calculated from the [O II]$\lambda 3727$/Hβ emission line ratio and assuming $T_e(O^+)=T_e(N^+)$ with $T_e(N^+)$ estimated from the empirical relation given by Eq. 3 when the [N II]$\lambda 5755$ auroral emission-line measurement is not available.

To derive ICF($O^+ + O^{2+}$) it is necessary to calculate the He^+/H^+ and He^{2+}/H^+ ionic abundances (e.g. Torres-Peimbert & Peimbert 1977; Izotov et al. 2006; Flury & Moran 2020), which is not possible because in most of the AGN spectra from our sample, the helium recombination line $\lambda 4686$ Å is not measured. Therefore, for consistency, the ICF($O^+ + O^{2+}$) is assumed to have a value of 1.50 for all objects, which is an average value derived by Dors et al. (2022), who found ICF values ranging from 1.30 to 1.70 for a sample of 65 local ($z \lesssim 0.2$) Sy 2s. This ICF value translates into an abundance correction of ~ 0.2 dex, i.e., somewhat higher than the uncertainty (~ 0.1 dex) of abundances usually relied on for the T_e-method (e.g. Kennicutt et al. 2003; Hägele et al. 2008).

3.2.2 Sulphur abundance

The S^+/H^+ ionic abundance for each object of our sample was derived by using the [S II]$(\lambda 6716 + \lambda 6731)$/H$\beta$ line intensities ratio and assuming $T_e(S^+)=T_e(N^+)$, where $T_e(N^+)$ was calculated from Eq. 3 when the [N II]$\lambda 5755$ auroral emission-line measurement is not available. Due to the similarity between the ionization potentials of S^+ and N^+ (23.33 eV and 29.60 eV, respectively) these ions are approximately located in the same gas region and the use of a common temperature for both is a good approach as largely used in SF chemical abundance studies (e.g. Kennicutt et al. 2003). However, Rogers et al. (2021), who compared SF direct estimates of $T_e(S^+)$ [derived from $RAS2=$[S II]$(\lambda 6716 + \lambda 6731)/(\lambda 4068 + \lambda 4074)$] with $T_e(N^+)$ [derived from $RN2=$[N II]$(\lambda 6548 + \lambda 6584)/(\lambda 5755)$], found somewhat higher $T_e(S^+)$ values than $T_e(N^+)$, with an intrinsic dispersion of ~ 950 K between these temperatures. Unfortunately, $RAS2$ values for Sy 2 are rarely found in the literature thus far, which makes it impossible to verify whether any of these conclusions also apply to AGNs.

Similarly, the S^{2+}/H^+ was derived by using the [S III]$\lambda 9069$/Hβ line intensities ratio listed in Table A1 and the $T_e(S^{2+})$ values from Eq. 4 when the $RS3$ line ratio is not available. The uncertainties associated with the sulphur ionic estimates is mainly due to the error in the measurements of the emission-line fluxes and the uncertainties in the temperature values. In Table A3, the sulphur ionic abundance values for each object of the sample are listed.

The total sulphur abundance in relation to the hydrogen one was considered to be

$$\frac{S}{H} = \text{ICF}(S^+ + S^{2+}) \times \left[\frac{S^+}{H^+} + \frac{S^{2+}}{H^+}\right], \quad (6)$$

where ICF($S^+ + S^{2+}$) is the Ionization Correction Factor for sulphur. Since AGNs have harder ionizing sources than typical SFs (e.g. Feltre et al. 2016), it is expected that the gas phase of these objects contains the presence of ions with higher ionization level than S^{2+}. In fact, [S VIII]$\lambda 9910$ and [S IX]$\lambda 12520$ emission lines were observed in large number of AGNs in the sample presented by Riffel et al. (2006). However, measurements of S^{3+} lines (e.g. [S IV]10.51μm) are not available in the literature, which makes it impossible for the derivation of an empirical ICF(S) for AGNs, such as derived for SFs by Dors et al. (2016).
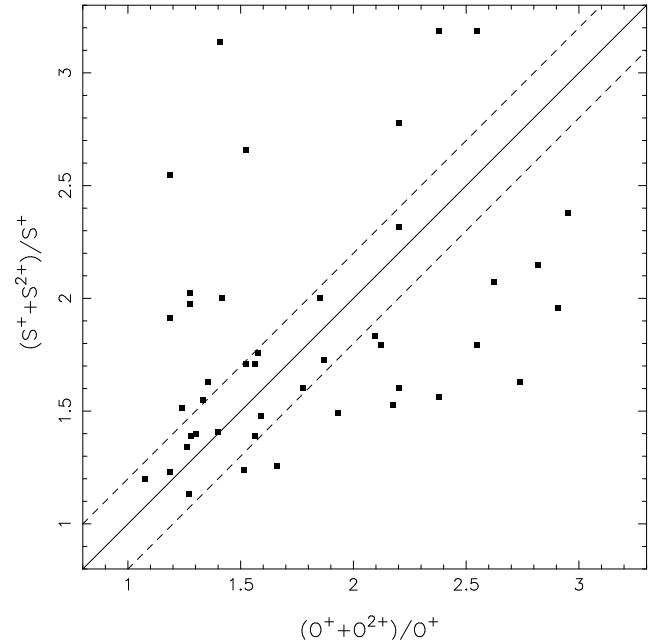
Figure 6. Sulphur versus oxygen ionic abundance ratios for our sample of objects (see Sect. 2) calculated via the T_e-method (see Sect. 3). Solid line represents the equality between the estimates. Dashed lines correspond to the deviation of 20 % from the one-one relation representing the mean error in the ionic abundance estimations.

The first ICF for sulphur (likewise for other elements) was proposed for SFs by Peimbert & Costero (1969) and it is given by

$$\text{ICF}(S^+ + S^{2+}) = \frac{S^+ + S^{2+}}{S^+} = \frac{O^+ + O^{2+}}{O^+}. \quad (7)$$

Rogers et al. (2021) tested the application of this ICF for SFs (see also Díaz & Zamora 2022) and pointed out that it is particularly reliable for low ionization degree, i.e. when O^+ zone is more dominant than the O^{2+} zone [(O^+/O) > 0.6]. Hitherto, there has not been sulphur ICFs for AGNs in the literature and it is unknown if the above relation is completely valid for this object class. Therefore, in order to ascertain whether the sulphur ICF can be applied to Sy 2s, we performed a simple test to verify the equality indicated in Eq. 7. The ionic ratios for our sample are plotted in Fig. 6, where the black solid line represents the equality between the estimates, while the dashed lines represent the deviations of 20 % from the one-one relation. It can be seen that, despite the scattering, most of the ionic abundance ratio estimates are located around of the one-one relation. Thus, we assumed as valid the Eq. 7 for NLR sulphur abundance estimates.

Ionic and total oxygen and sulphur abundance estimates derived through the T_e-method together with the sulphur ICFs for each object in our sample are listed in Table A3.

4 RESULTS & DISCUSSION

4.1 Temperature estimates

Recent studies of spatially resolved central parts of galaxies have uncovered the temperature structure of a few AGNs. For instance, Revalski et al. (2021), using Hubble Space Telescope and Apache Point Observatory spectroscopy, obtained direct estimates of $T_e(O^{2+})$ along the radius of the Sy 2 nucleus of Mrk 78 and found temperatures in the range 10 000-15 000 K, with no systematic variation (see also

Revalski et al. 2018a,b). Riffel et al. (2021c) used Gemini GMOS-IFU observations of three luminous nearby Seyfert galaxies (Mrk 79, Mrk 348 and Mrk 607) and estimated $T_e(O^{2+})$ fluctuations in the inner 0.4–1.1 kpc region of these galaxies. These authors found temperature fluctuations similar to those derived in SFs and PNe. Despite the revelations provided by these recent studies, an advance in the understanding of the temperature structure of AGNs, additional point-to-point or integrated T_e estimates through distinct emission lines [e.g. [S III]$(\lambda 9069 + \lambda 9532)/\lambda 6312$ and [N II]$(\lambda 6548 + \lambda 6584)/\lambda 5755$] are rare in the literature, prompting further investigation of the AGN temperature structure. Thus, our temperature estimates provide valuable knowledge to the nature of NLRs.

A large number of AGNs present gas outflows (e.g. Riffel et al. 2020; Armus et al. 2022), shocks (e.g. Aldrovandi & Contini 1984; Dopita & Sutherland 1995; Dors et al. 2021) and neutral gas reservoirs which can coexist with the ionized gas (e.g. García-Burillo et al. 2014) and, in combination with the hard ionization source (e.g. Feltre et al. 2016), trend to produce a more complex gas structure than that of SFs (e.g. Hägele et al. 2006; García-Benito et al. 2010; Pérez-Montero et al. 2011; Monreal-Ibero et al. 2012; Durré & Mould 2018). However, complex temperature structures can also be observed in SFs (e.g., Dopita et al. 2005; Jin et al. 2022) produced, for instance, by starburst-driven outflows cooling (e.g. Danehkar et al. 2022). On the scenario where distinct physical processes drive the gas structure, it is expected that temperature relations of AGNs tend to differ from the ones derived for SFs. In order to test this hypothesis, in Fig. 7, we compare our Sy 2 temperature estimates and empirical relations (Eqs. 3 and 4) with those derived for SFs by the following authors:

(i) Hägele et al. (2006): these authors used their own high quality spectra of H II galaxies and a large literature compilation of H II galaxies, Giant Extragalactic H II regions (GHRs), Galactic H II regions, and H II regions from the Magellanic Clouds performed by Pérez-Montero et al. (2006) to analyse the relation between $T_e(O^{2+})$ and $T_e(S^{2+})$ values derived using the T_e-method (see Fig. 7 of Hägele and collaborators). Their linear fitting to the complete sample gave the relation:

$$t_e(S^{2+}) = 1.19(\pm 0.08) \times t_e(O^{2+}) - 0.32(\pm 0.10), \quad (8)$$

which has a validity range of $0.70 \lesssim t_e(O^{2+}) \lesssim 2.0$.

(ii) Rogers et al. (2021): the estimates by these authors include temperature values obtained for a large number of disk H II regions in the spiral galaxy NGC 2403 using the T_e-method. These estimates combined with those of H II regions in four spiral galaxies (see Fig. 3 by Rogers et al. 2021) resulted in the relations:

$$t_e(N^+) = 0.79(\pm 0.14) \times t_e(O^{2+}) + 0.16(\pm 0.13), \quad (9)$$

and

$$t_e(S^{2+}) = 1.58(\pm 0.17) \times t_e(O^{2+}) - 0.57(\pm 0.16), \quad (10)$$

which are valid for $0.70 \lesssim t_e(O^{2+}) \lesssim 1.5$.

(iii) Arellano-Córdova & Rodríguez (2020): these authors compiled emission line intensities of H II regions from the literature to explore the behaviour of the $T_e(N^+)$-$T_e(O^{2+})$ temperature relation. These authors found that this relation has a dependence on the gas ionization degree, which is traced by the line ratio $P = ([O III]\lambda 4959 + \lambda 5007)/[O II]\lambda 3727 + [O III]\lambda 4959 + \lambda 5007$. The following relations, which hold for $0.60 \lesssim t_e(O^{2+}) \lesssim 1.7$, were derived:
For $P < 0.5$

$$\frac{1}{t_e(N^+)} = \frac{0.54(\pm 0.05)}{t_e(O^{2+})} + 0.52(\pm 0.08) \quad (11)$$

and for $P > 0.5$

$$\frac{1}{t_e(N^+)} = \frac{0.61(\pm 0.04)}{t_e(O^{2+})} + 0.36(\pm 0.04). \quad (12)$$

(iv) Garnett (1992): this author, by using the photoionization model results derived by Stasińska (1982), proposed the relation

$$t_e(S^{2+}) = 0.83 \times t_e(O^{2+}) - 0.17, \quad (13)$$

valid for $0.4 \lesssim t_e(O^{2+}) \lesssim 1.8$.

(v) Pérez-Montero & Contini (2009): using photoionization model results built through the CLOUDY code these authors deduce a relation between $T_e(O^{2+})$ and $T_e(N^+)$ given by:

$$t_e(N^+) = \frac{1.85}{t_e(O^{2+})^{-1} + 0.72} \quad (14)$$

with a valid range $0.60 \lesssim t_e(O^{2+}) \lesssim 1.8$.

In Fig. 7, the above relations are compared with our estimates and our own temperature relations. It can be seen in the bottom panel of Fig. 7 that Sy 2 nuclei present similar $T_e(N^+)$ values for a given $T_e(O^{2+})$ to those from SFs. Otherwise, in Fig. 7, upper panel, $T_e(S^{2+})$ NLR estimates are higher than those in SFs. This result indicates that NLRs have a hotter high ionization zone than the one in SFs. This is probably due to the known fact that SEDs of AGNs are harder than the ones of SFs. Moreover, gas shocks present in AGNs can produce a very distinct temperature structure than that in SFs, where shocks have a little influence. In fact, Dors et al. (2021) built detailed composite models of photoionization and shock ionization based on the SUMA code (Viegas-Aldrovandi & Contini 1989) to reproduce optical emission lines emitted by NLRs of 244 Sy 2 nuclei. Their models predicted an abrupt increase in temperature near the shock front, reaching values of $\sim 10^5$ K, mainly in shock-dominated objects (see Fig. 14 by Dors et al. 2021). In summary, our temperature estimates support the scenario where AGNs have complex spatial distributions of gas-temperature and a variety of mechanisms can drive the temperature and ionization (e.g., see Bedregal et al. 2009; Busch et al. 2016; Durré & Mould 2018; Fazeli et al. 2019).

4.2 Sulphur abundances

According to the inside-out scheme, galaxies begin to form stars in their inner regions before the outer ones (e.g. Samland et al. 1997; Portinari & Chiosi 1999; Boissier & Prantzos 2000; Sommer-Larsen et al. 2003; Mollá & Díaz 2005; Nelson et al. 2012, 2016; Vincenzo & Kobayashi 2018) producing radial metallicity gradients with negative slopes (i.e. the metalicity decreases with the increase of the galactocentric distance, e.g. Pilyugin et al. 2004). Thus, due to the location of AGNs in galactic disks, they are expected to have high abundance of heavy elements; in other words, AGNs with low abundances are barely found in the local universe (e.g. Groves et al. 2006; Izotov & Thuan 2008; Izotov et al. 2010; Kawasaki et al. 2017; Dors et al. 2020a). However, AGNs seem to have a more complex cosmic chemical evolution than SFs. For instance, Matteucci & Padovani (1993), by means of self-consistent models of galaxy evolution, showed that AGNs in galaxies around the lifetime of 10^9 years ($z \sim 5$) reach an abundance of elements divided into two classes: (*i*) elements with 2-3 times the solar abundance (C, Ne, O and Mg) and (*ii*) the ones with abundances ranging from 5 to 10 times the solar abundance (N, Ni and Fe). Conversely, low abundance or metallicity have been derived at high redshift from SFs (see Curti et al. 2022 and references therein). Despite the fact that Matteucci & Padovani (1993) did not
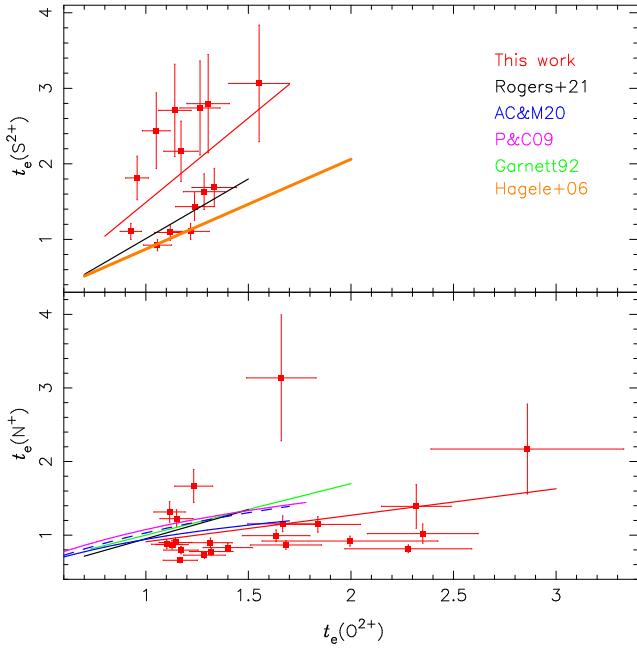
Figure 7. Same as Fig. 5 but comparing our temperature estimates (red points) and temperature relations (red lines represented by Eqs. 3 and 4) with relations obtained from SFs. Orange solid line plots the empirical relation (Eq. 8) obtained by Hägele et al. (2006) using direct temperature estimates for a large sample of H II galaxies, giant extragalactic H II regions, Galactic H II regions, and H II regions from the MCs. Black solid lines represent the empirical relations (Eqs. 9 and 10) based on direct estimates of disk H II regions by Rogers et al. (2021). Blue dashed and solid lines, shown only in bottom panel, represent empirical relations for $P < 0.5$ and for $P > 0.5$, respectively, based on data compiled from literature by Arellano-Córdova & Rodríguez (2020). P is defined as $([\text{O\,III}]\lambda4959 + \lambda5007)/[\text{O\,II}]\lambda3727 + [\text{O\,III}]\lambda4959 + \lambda5007)$. Green and pink lines represent the theoretical relations derived by Garnett (1992, Eq.13) and Pérez-Montero & Contini (2009, Eq.14), respectively.

consider sulphur (an α-element), its abundance would increase similarly to the oxygen abundance, i.e. the expectation will be a constant S/O abundance ratio.

Optical surveys, such as SDSS, have made plenty of AGNs spectroscopic data available, which make the determinations of quantitative sulphur abundance possible in this class of objects. In this sense, we present a detailed analysis of sulphur abundance from our Sy 2 sample and a comparison with some previous results obtained from SFs. In view of that, we consider the following SF estimates which relied on the T_e-method:

• Hägele et al. (2006): these authors presented calculations for several heavy elements from a sample of H II galaxies (33 objects) and Giant H II Regions (34 objects) by using the T_e-method. In particular, for the sulphur abundance, they assumed the ICF approach proposed by Barker (1980) with the α exponent equal to 2.5. Following the same procedure, Hägele et al. (2008, 2011, 2012) studied another 11 H II galaxies and knots belonging to this kind of objects that we include in our control sample.

• CHAOS project: the Chemical Abundances Of Spirals (CHAOS[5], Berg et al. 2015) combines the power of the Large Binocular Telescope (LBT) with the broad spectral range and sensitivity of the Multi Object Double Spectrograph (MODS) to derived abundances, which relied on the T_e-method, for a large sample of H II

---

[5] https://www.danielleaberg.com/chaos

regions in spiral galaxies. Taking these valuable data into account, we consider abundance estimates for 135 disk H II regions located in NGC 5457, NGC 3184 and NGC 2403 by Croxall et al. (2016), Berg et al. (2020) and Rogers et al. (2021), respectively. These authors adopted the sulphur ICF given by Eq. 7 for $(\text{O}^+/\text{O}) \gtrsim 0.6$ and the theoretical ICF from Thuan et al. (1995) when $(\text{O}^+/\text{O}) \lesssim 0.6$.

Along this section, we have used the SF abundance estimates from the above authors as benchmark. We emphasize that any selection effect, such as that which may arise as a result of the existence of auroral lines in spectra, will be present in both our AGN sample and the SF sample taken from the literature.

Our sulphur ICFs for the Seyfert galaxies (listed in Table A3) indicate values between ~ 1.1 and ~ 3.0, with an averaged value of 1.44, i.e. about 45% of the sulphur is in higher ionization stages than S^{2+}. We found an ICF value higher than 2.0 for only two objects: 2.02 and 2.94 for Mrk 573 and NGC 7674, respectively. Interestingly, for the most extreme ICF value, i.e. for NGC 7674, Kharb et al. (2017), by using radio long baseline interferometry, hinted that this object hosts a Binary Supermassive Black Hole (for a different conclusion see Breiding et al. 2022). Moreover, additional evidence that this object has a hard ionizing spectra is the presence of emission lines of high ionization ions [Ne v]$\lambda3346$, $\lambda3426$, as observed by Kraemer et al. (1994). In any case, even if this object is ruled out from the average ICF calculations, a similar value (1.40) is obtained. In order to compare our sulphur ICF values with those from SFs, we consider the ICFs derived by Hägele et al. (2006) and from the CHAOS project. In the left panel of Fig. 8, the distribution of sulphur ICFs for Sy 2s and SFs are shown, where it can be seen that a good agreement exist among them, even though the GHRs present a distribution peak at lower values. It is worth to be noted that most of the objects ($\sim 90\%$) belonging to the distinct object classes present sulphur ICFs lower than ~ 2. The range and average of the ICFs for our sample of Sy 2, H II galaxies, GHRs and disk H II regions are presented in Table 4 showing that the different samples have similar ICF values. Therefore, despite the fact that Sy 2s have a harder ionizing source than SFs, these two distinct object classes have similar sulphur ionic fractions.

Concerning the total sulphur abundance, in the right panel of Fig. 8, we present the S/H abundance distribution for our sample of Sy 2 nuclei, H II galaxies and GHRs from Hägele et al. (2006, 2008, 2011, 2012) and for disk H II regions from the CHAOS project. Also in this plot, the sulphur solar abundance $12 + \log(\text{S/H})_\odot = 7.27$ derived by Grevesse & Sauval (1998) is represented by the dashed line. We note that the Sy 2s present an intermediate S/H distribution between that of GHRs and the disk H II regions, while H II galaxies tend to present lower sulphur abundances. In Table 4 the range and S/H average values for our AGN sample and for the SF benchmark sample are listed. The Sy 2s present S/H values in the range of $6.2 < 12 + \log(\text{S/H}) < 7.5$ and considering the sulphur solar value as $12+\log(\text{S/H})_\odot = 7.26$ (Grevesse & Sauval 1998), represents $0.1 < (\text{S/S}_\odot) < 1.8$, where most of the objects (40/45) have subsolar sulphur abundance. This result can be biased due to the fact that we selected only objects which have the [S III]$\lambda9069$ and auroral line [O III]$\lambda4363$ measured, resulting (see Table 4) only in Sy 2s with O/H values in the range $8.0 \lesssim 12 + \log(\text{O/H}) \lesssim 9.1$ or $0.2 \lesssim (\text{Z/Z}_\odot) \lesssim 2.6$, adopting the solar oxygen value of $12 + \log(\text{O/H})_\odot = 8.69$ (Allende Prieto et al. 2001). Dors et al. (2020a), who considered a sample of 463 confirmed Seyfert 2 AGNs ($z \lesssim 0.4$) and used distinct methods which did not necessarily required auroral lines, found values in the range $7.1 \lesssim 12 + \log(\text{O/H}) \lesssim 9.2$ or $0.02 \lesssim (\text{Z/Z}_\odot) \lesssim 3.2$. Therefore, lower and higher S/H abundances
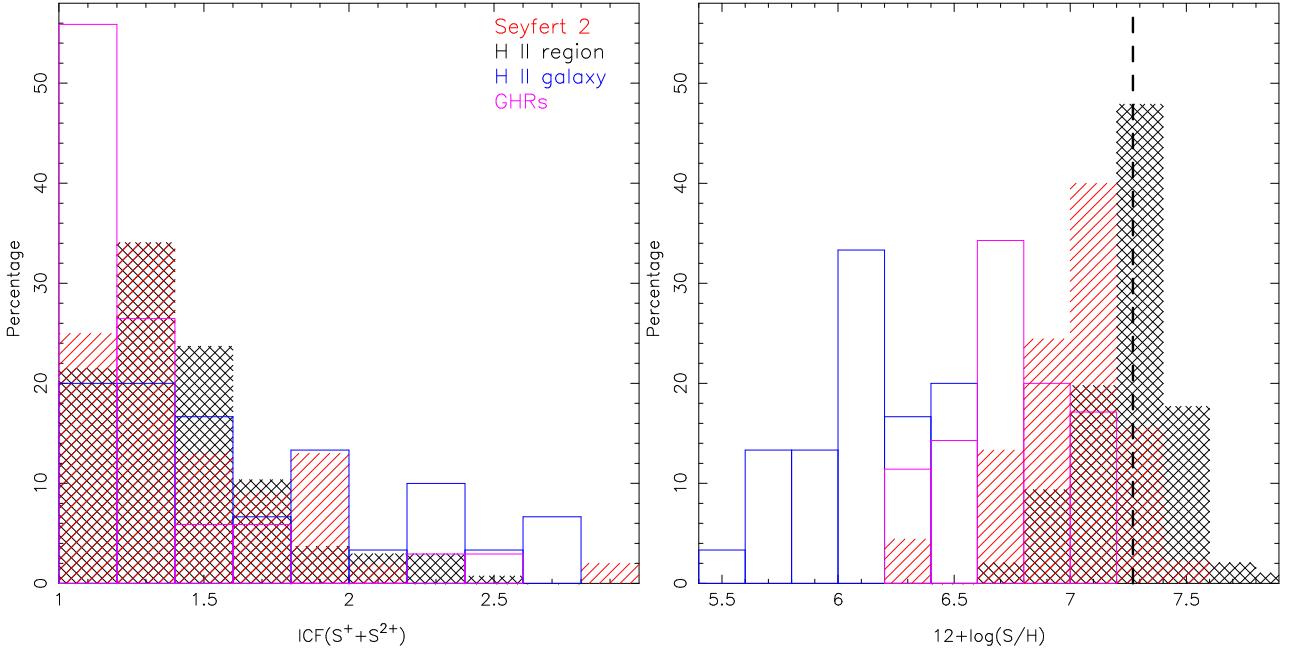
Figure 8. Left panel: distributions for the sulphur ICF (see Sect. 3.2.2). Red distribution is derived from our Sy 2 sample by using Eq. 7 (values listed in Table A3). Black distribution is derived by using values from disk H II region estimates (i.e. results from CHAOS project) assuming Eq. 7 for $(O^+/O) \gtrsim 0.6$ and the theoretical ICF from Thuan et al. (1995) when $(O^+/O) \lesssim 0.6$. Blue distribution corresponds to H II galaxies values from Hägele et al. (2006, 2008, 2011, 2012) and pink distribution corresponds to GHRs from Hägele et al. (2006), and for both kind of objects the approach proposed by Barker (1980) was used. Right panel: distributions for the sulphur abundance. Dashed line represents the sulphur solar abundance $12 + \log(S/H)_\odot = 7.27$ derived by Grevesse & Sauval (1998). The color code is the same as in left panel.

Table 4. Range and average sulphur ICF, S/H, O/H, and S/O abundance values for our sample of Sy 2s, disk H II regions, H II galaxies, and Giant H II regions.

Object type	ICF($S^+ + S^{2+}$) Range	Average	12+log(S/H) Range	Average	12+log(O/H) Range	Average	log(S/O) Range	Average	Ref.
Sy 2	1.1 - 3.0	1.44	6.2 - 7.5	6.98 ± 0.25	8.0 - 9.1	8.71 ± 0.24	$-2.4 - -1.3$	-1.64 ± 0.20	1
H II region	1.1 - 2.5	1.43	6.2 - 7.9	7.11 ± 0.28	7.8 - 8.9	8.47 ± 0.19	$-1.7 - -0.9$	-1.35 ± 0.15	2
H II galaxy	1.0 - 2.8	1.66	5.5 - 6.6	6.10 ± 0.27	7.0 - 8.2	7.79 ± 0.30	$-2.0 - -1.4$	-1.67 ± 0.15	3,4
GHR	1.0 - 2.5	1.26	6.2 - 7.2	6.73 ± 0.24	7.6 - 8.6	8.12 ± 0.23	$-1.9 - -0.7$	-1.38 ± 0.30	4

(1) This work. (2) Croxall et al. (2016), Berg et al. (2020) and Rogers et al. (2021). (3) Hägele et al. (2008, 2011, 2012). (4) Hägele et al. (2006).

would be probably derived in the sample if the data by Dors et al. (2020a) could be taken into account. In any case, the abundance estimates from the CHAOS project comprises inner disk H II regions, therefore, it is expected that these objects and Sy 2 nuclei would have similar S/H abundances, when a large sample of objects is considered. Interestingly, the maximum S/H value ($\sim$ 7.9 dex) is derived for disk H II regions while sulphur abundances in Sy 2s reach up to $\sim$ 7.5 dex. This result points to a distinct chemical enrichment of the ISM near the AGNs in comparison to that of the innermost disk H II regions. We emphasize that a more detailed comparison taking into account SFs and AGNs located in galaxies with similar mass (see do Nascimento et al. 2022) is need to confirm this result.

In Fig. 9, we show a plot of the S/H versus O/H abundances for our Sy 2 sample and for the SF benchmark. Also in this figure, the range of the S/H values derived from the photoionization models by Storchi-Bergmann & Pastoriza (1990) and considering a larger sample of AGNs than our data, is indicated. Berg et al. (2020) summarized the radial sulphur gradients (and the gradients for other elements) in four spiral galaxies from the CHAOS project, which are represented by

$$12 + \log(S/H) = grad(S) \times R + Y_0(S), \qquad (15)$$

where $grad(S)$ is the value of the slope of the sulphur gradient, R is the radial galactic distance and $Y_0(S)$ is the extrapolated value of S/H gradient to the galactic center $R = 0$. The range of $Y_0(S)$ derived by Berg et al. (2020) is also represented in Fig. 9. We note that, for a given O/H value, in general Sy 2s present lower S/H values than the majority of disk H II regions and than those from extrapolated gradients. Again, this discrepancy can be due to the distinct chemical evolution of AGNs and SFs or even due to the small AGN sample (the sample contains only 45 objects). H II galaxies and GHRs present lower S/H and O/H abundances in comparison with the Sy 2s, which indicate that the former objects are less chemically evolved than the latter. Finally, the model results by Storchi-Bergmann & Pastoriza (1990) predicted, on average, higher ($\sim$ 0.3 dex) S/H values than those derived by using the T_e-method for Sy 2s. This discrepancy can be partly due to the known problem of photoionization models overestimating abundances in comparison to the T_e-method. In fact, Dors et al. (2020b) showed that direct temperature estimates of $T_e(O^{2+})$ are higher (up to 11 000 K) than those predicted by photoionization models, which translates into an overestimate of the O/H abundance of up to $\sim$ 1 dex (with an average value of $\sim$ 0.2 dex)
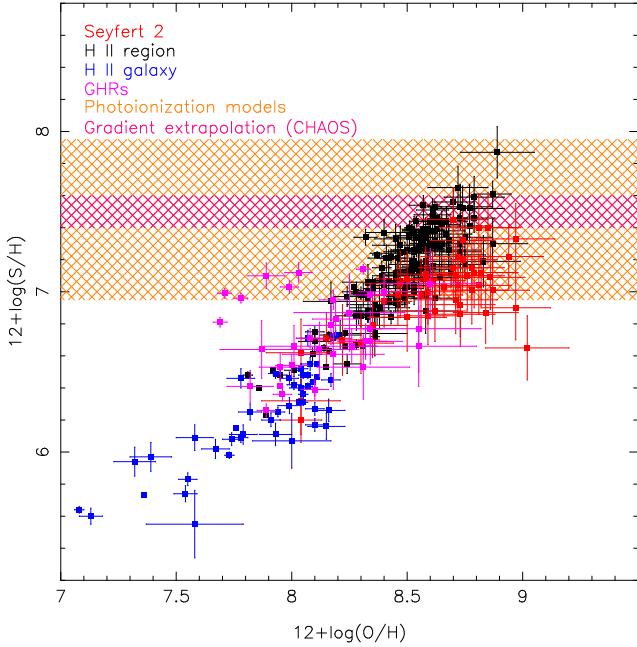
Figure 9. Relation between the total sulphur and oxygen abundances [12+log(S/H) vs. 12+log(O/H)]. Red points represent our Sy 2 nuclei direct estimates. Black points represent estimates from disk H II regions also obtained through the T_e-method from the CHAOS project. Pink points represent GHRs estimated from Hägele et al. (2006) and blue ones those estimates for H II galaxies from Hägele et al. (2006, 2008, 2011, 2012). The orange hatched area represents the range of S/H values inferred through photoionization models for a sample of 177 Seyfert galaxies by Storchi-Bergmann & Pastoriza (1990). The magenta hatched area represents the range of S/H values obtained from the extrapolation of radial abundance gradients to central parts of four (NGC 0628, NGC 5194, NGC 5457, NGC 3184) spiral galaxies by Berg et al. (2020).

by the photoionization models. In order to ascertain if the temperature problem also exists in the sulphur temperatures, in Fig. 10, we compare our direct temperature estimates (shown in Fig. 4) with temperature predictions by the photoionization models built with the CLOUDY code by Carvalho et al. (2020) taking into account a wide range of NLR nebular parameters:

- Metallicity: $(Z/Z_\odot) = 3.0, 2.0, 1.0, 0.75, 0.5,$ and 0.2.
- Electron density: N_e (cm^{-3}) = 3000, 1500, 500, 100.
- Ionization parameter (U): $\log U$ ranging from -1.5 to -3.5, with step of 0.5 dex.
- Spectra Energy Distribution (SED): the SED is parametrized by the continuum between 2 keV and 2500Å (Tananbaum et al. 1979) and it is described by a power law with a spectral index α_{ox}=−0.8, −1.1 and −1.4.

In Fig. 10, it can be seen that similar to oxygen temperatures (see Dors et al. 2020b) direct temperature estimates for S$^+$ and S^{2+} are higher than those predicted by AGN photoioinization models[6]. Thus, this result explains the discrepancy between the sulphur abundance inferred by the photoionization models built by Storchi-Bergmann & Pastoriza (1990) and those calculated from our sample by using the T_e-method.

Finally, in Fig. 11, we show a plot of log(S/O) versus 12+log(O/H),

---

[6] Model temperatures values in Fig. 10 correspond to the mean temperature for S$^+$ and S^{2+} over the nebular AGN radius times the electron density.
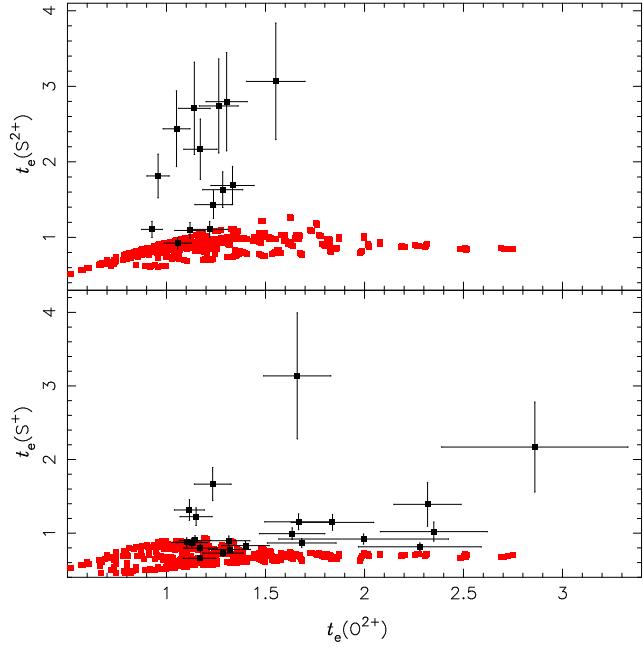
Figure 10. Temperatures (in units of 10^4 K) for the S$^+$ (bottom panel) and S^{2+} (upper panel) versus the temperature for O^{2+}. Black points are Sy 2 direct estimations which relied on auroral lines (see Sect. 4.1). Red points are temperature predictions by AGN photoionization models built with the CLOUDY code by Carvalho et al. (2020).

which compares our direct abundance estimates with the SF benchmark. Considering the estimates of all objects (AGN+SF), we provide the following relation

$$\log(S/O) = +0.06(\pm 0.03) \times [12 + \log(O/H)] - 1.94(\pm 0.33), \quad (16)$$

with the Pearson coefficient parameters ($R = 0.09 \pm 0.07$ and *p-value* = 0.24), i.e. there is no correlation between the estimations. Thus, our estimates combined with those from a large sample of SFs suggest that S/O is constant over a wide range of O/H, as found by recent results from the CHAOS project (see Rogers et al. 2021 and references therein). However, in Fig. 11, it can be seen that there is a clear trend of S/O values of Sy 2 decreasing with O/H in the high metallicity regime. The same behaviour was found from H II regions, for instance, by Dors et al. (2016) and Díaz & Zamora (2022).

It is worth to mention that emission lines of AGNs, such as [S III]λ9069, λ9532 and auroral lines (mainly [N II]λ5755 and [S III]λ6312) are either measured with low S/N (∼ 2) or unavailable in the literature (e.g., see Koski 1978; Dopita et al. 2015). This implies that chemical abundance studies of AGNs are difficult to be carried out and, even when it is possible to determine the abundance directly, higher (a factor of ∼ 2, see Fig 9) abundance errors in comparison with those of SFs are derived. The next generation of telescopes, such as the Giant Magellan, European Extremely Large, and Thirty Meter Telescopes, will provide higher S/N measurements of weak AGN emission lines and will allow a breakthrough in our understanding of the chemical abundance in AGNs and objects with very high metallicity.

5 CONCLUSIONS

We have used observations of the intensities of narrow emission lines in the spectral interval 3000 < λ(Å) < 9100 of sample of
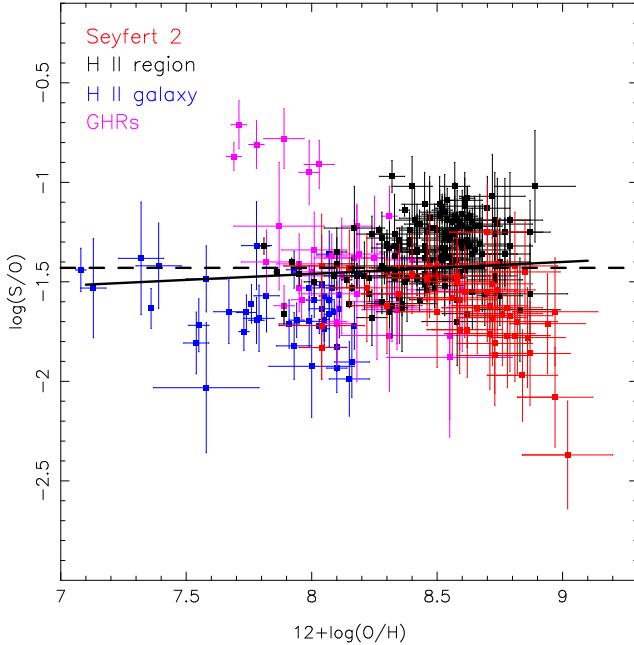
Figure 11. Relation between log(S/O) and 12+log(O/H). Red points represent our Sy 2 nuclei direct estimates. Pink points represent direct estimates for GHRs from Hägele et al. (2006). Black points represent estimates from disk H II regions obtained also through T_e-method by Berg et al. (2020). Blue points represent direct estimates for H II galaxies by Hägele et al. (2006, 2008, 2011, 2012). Dashed line represents the solar value of $\log(S/O)_\odot = -1.43$. Solid line represents the linear regression considering all the estimates given by Eq. 16.

45 nearby ($z \lesssim 0.08$) Seyfert 2 nuclei taken from SDSS DR17 and other compilations from the literature to perform direct estimations of electron temperatures through the T_e-method and estimates of sulphur and oxygen abundances relative to hydrogen. These estimates were compared with those from local star-forming regions, i.e. disk H II regions, H II galaxies and Giant H II Regions, whose abundance estimates were compiled from the literature. Regarding the electron temperatures, we found that Seyfert 2 and star-forming regions have similar temperature in the gas regions where most S^+ is located. However, this result is not derived for the zones where most S^{2+} is located: S^{2+} electron temperatures are higher ($\sim 10\,000$ K) from Seyfert 2 than from star-forming regions. We interpret this result as, probably, due to the known feature of SEDs of AGNs are harder than that of SFs, producing a hotter gas in the innermost narrow line region of AGNs. For our sample of Seyfert 2, we derived total sulphur abundances in the range of $6.2 \lesssim 12 + \log(S/H) \lesssim 7.5$ or $0.1 \lesssim (S/S_\odot) \lesssim 1.8$. The Seyfert 2 sulphur abundances are lower by a factor of ~ 0.4 dex than those derived for SFs with similar metallicities. This discrepancy can be interpreted as due to a distinct chemical enrichment of the ISM near the AGNs in comparison to that of the SFs. The relation between S/O and O/H abundance ratios derived from our Seyfert 2 nuclei sample presents an abrupt (~ 0.5 dex) decrease with the increase of O/H for the high metallicity regime $[12 + \log(O/H) \gtrsim 8.7)]$, which is not derived from star-forming regions. However, when our Sy 2 estimates are combined with those from a large sample of star-forming regions, we did not find any dependence between S/O and O/H, supporting the idea that sulphur and oxygen are produced by stars with similar mass range and that the Initial Mass Function is universal.

DATA AVAILABILITY

The data underlying this article will be shared on reasonable request to the corresponding author.

REFERENCES

Abazajian K., et al., 2005, AJ, 129, 1755
Abazajian K. N., et al., 2009, ApJS, 182, 543
Abdurro'uf et al., 2022, ApJS, 259, 35
Aihara H., et al., 2011, ApJS, 193, 29
Aldrovandi S. M. V., Contini M., 1984, A&A, 140, 368
Allende Prieto C., Lambert D. L., Asplund M., 2001, ApJ, 556, L63
Allende Prieto C., Barklem P. S., Lambert D. L., Cunha K., 2004, A&A, 420, 183
Aller L. H., Czyzak S. J., 1983, ApJS, 51, 211
Alloin D., Bica E., Bonatto C., Prugniel P., 1992, A&A, 266, 117
Arellano-Córdova K. Z., Rodríguez M., 2020, MNRAS, 497, 672
Arellano-Córdova K. Z., Esteban C., García-Rojas J., Méndez-Delgado J. E., 2020, MNRAS, 496, 1051
Arellano-Córdova K. Z., et al., 2022, ApJ, 935, 74
Armah M., et al., 2021, MNRAS, 508, 371

Armus L., et al., 2022, arXiv e-prints, p. arXiv:2209.13125
Barker T., 1980, ApJ, 240, 99
Bedregal A. G., Colina L., Alonso-Herrero A., Arribas S., 2009, ApJ, 698, 1852
Berg D. A., Skillman E. D., Garnett D. R., Croxall K. V., Marble A. R., Smith J. D., Gordon K., Kennicutt Robert C. J., 2013, ApJ, 775, 128
Berg D. A., Skillman E. D., Croxall K. V., Pogge R. W., Moustakas J., Johnson-Groh M., 2015, ApJ, 806, 16
Berg D. A., Pogge R. W., Skillman E. D., Croxall K. V., Moustakas J., Rogers N. S. J., Sun J., 2020, ApJ, 893, 96
Bergvall N., Johansson L., Olofsson K., 1986, A&A, 166, 92
Bernard-Salas J., Pottasch S. R., Gutenkunst S., Morris P. W., Houck J. R., 2008, ApJ, 672, 274
Bianchi S., Chiaberge M., Evans D. A., Guainazzi M., Baldi R. D., Matt G., Piconcelli E., 2010, MNRAS, 405, 553
Binette L., Matadamas R., Hägele G. F., Nicholls D. C., Magris C. G., Peña-Guerrero M. Á., Morisset C., Rodríguez-González A., 2012, A&A, 547, A29
Bogdán Á., Kraft R. P., Evans D. A., Andrade-Santos F., Forman W. R., 2017, ApJ, 848, 61
Boissier S., Prantzos N., 2000, MNRAS, 312, 398
Bonifacio P., Caffau E., Centurión M., Molaro P., Vladilo G., 2001, MNRAS, 325, 767
Breiding P., Burke-Spolaor S., An T., Bansal K., Mohan P., Taylor G. B., Zhang Y., 2022, ApJ, 933, 143
Busch G., et al., 2016, A&A, 587, A138
Caffau E., Bonifacio P., Faraggiana R., François P., Gratton R. G., Barbieri M., 2005, A&A, 441, 533
Cardaci M. V., Santos-Lleó M., Krongold Y., Hägele G. F., Díaz A. I., Rodríguez-Pascual P., 2009, A&A, 505, 541
Cardaci M. V., Santos-Lleó M., Hägele G. F., Krongold Y., Díaz A. I., Rodríguez-Pascual P., 2011, A&A, 530, A125
Cardelli J. A., Clayton G. C., Mathis J. S., 1989, ApJ, 345, 245
Carvalho S. P., et al., 2020, MNRAS, 492, 5675
Castro C. S., Dors O. L., Cardaci M. V., Hägele G. F., 2017, MNRAS, 467, 1507
Cavichia O., Costa R. D. D., Maciel W. J., Mollá M., 2017, MNRAS, 468, 272
Centurión M., Bonifacio P., Molaro P., Vladilo G., 2000, ApJ, 536, 540
Cerqueira-Campos F. C., Rodríguez-Ardila A., Riffel R., Marinello M., Prieto A., Dahmer-Hahn L. G., 2021, MNRAS, 500, 2666
Chevallard J., Charlot S., 2016, MNRAS, 462, 1415
Christensen T., Petersen L., Gammelgaard P., 1997, A&A, 322, 41
Cid Fernandes R., Mateus A., Sodré L., Stasińska G., Gomes J. M., 2005, MNRAS, 358, 363
Cid Fernandes R., Stasińska G., Schlickmann M. S., Mateus A., Vale Asari N., Schoenell W., Sodré L., 2010, MNRAS, 403, 1036
Cohen R. D., 1983, ApJ, 273, 489
Congiu E., et al., 2017, MNRAS, 471, 562
Costa Silva A. R., Delgado Mena E., Tsantaki M., 2020, A&A, 634, A136
Costa R. D. D., Uchida M. M. M., Maciel W. J., 2004, A&A, 423, 199
Croxall K. V., Pogge R. W., Berg D. A., Skillman E. D., Moustakas J., 2015, ApJ, 808, 42
Croxall K. V., Pogge R. W., Berg D. A., Skillman E. D., Moustakas J., 2016, ApJ, 830, 4
Curti M., et al., 2022, MNRAS,
Danehkar A., Oey M. S., Gray W. J., 2022, ApJ, 937, 68
Davies R. L., Rich J. A., Kewley L. J., Dopita M. A., 2014, MNRAS, 439, 3835
Delgado-Inglada G., Morisset C., Stasińska G., 2014, MNRAS, 440, 536
Denicoló G., Terlevich R., Terlevich E., 2002, MNRAS, 330, 69
Diamond-Stanic A. M., Rieke G. H., 2012, ApJ, 746, 168
Díaz Á. I., Zamora S., 2022, MNRAS, 511, 4377
Díaz Á. I., Terlevich E., Castellanos M., Hägele G. F., 2007, MNRAS, 382, 251
Dopita M. A., Sutherland R. S., 1995, ApJ, 455, 468
Dopita M. A., et al., 2005, ApJ, 619, 755
Dopita M. A., et al., 2015, ApJS, 217, 12

Dors O. L. J., Storchi-Bergmann T., Riffel R. A., Schimdt A. A., 2008, A&A, 482, 59
Dors O. L., Cardaci M. V., Hägele G. F., Krabbe Â. C., 2014, MNRAS, 443, 1291
Dors O. L., Pérez-Montero E., Hägele G. F., Cardaci M. V., Krabbe A. C., 2016, MNRAS, 456, 4407
Dors O. L. J., Arellano-Córdova K. Z., Cardaci M. V., Hägele G. F., 2017, MNRAS, 468, L113
Dors O. L., Agarwal B., Hägele G. F., Cardaci M. V., Rydberg C.-E., Riffel R. A., Oliveira A. S., Krabbe A. C., 2018, MNRAS, 479, 2294
Dors O. L., Monteiro A. F., Cardaci M. V., Hägele G. F., Krabbe A. C., 2019, MNRAS, 486, 5853
Dors O. L., et al., 2020a, MNRAS, 492, 468
Dors O. L., Maiolino R., Cardaci M. V., Hägele G. F., Krabbe A. C., Pérez-Montero E., Armah M., 2020b, MNRAS, 496, 3209
Dors O. L., Contini M., Riffel R. A., Pérez-Montero E., Krabbe A. C., Cardaci M. V., Hägele G. F., 2021, MNRAS, 501, 1370
Dors O. L., et al., 2022, MNRAS, 514, 5506
Durré M., Mould J., 2018, ApJ, 867, 149
Díaz A. I., Terlevich E., Vilchez J. M., Pagel B. E. J., Edmunds M. G., 1991, MNRAS, 253, 245
Espíritu J. N., Peimbert A., 2021, MNRAS, 508, 2668
Fang X., et al., 2018, ApJ, 853, 50
Fathivavsari H., Petitjean P., Ledoux C., Noterdaeme P., Srianand R., Rahmani H., Ajabshirizadeh A., 2013, MNRAS, 435, 1727
Fazeli N., Busch G., Valencia-S. M., Eckart A., Zajaček M., Combes F., García-Burillo S., 2019, A&A, 622, A128
Feltre A., Charlot S., Gutkin J., 2016, MNRAS, 456, 3354
Ferland G. J., Osterbrock D. E., 1986, ApJ, 300, 658
Ferland G. J., et al., 2013, Rev. Mex. Astron. Astrofis., 49, 137
Fernández-Ontiveros J. A., Spinoglio L., Pereira-Santaella M., Malkan M. A., Andreani P., Dasyra K. M., 2016, ApJS, 226, 19
Fernández V., Terlevich E., Díaz A. I., Terlevich R., 2019, MNRAS, 487, 3221
Flury S. R., Moran E. C., 2020, MNRAS, 496, 2191
Fox A., Richter P., Fechner C., 2014, A&A, 572, A102
Freitas I. C., et al., 2018, MNRAS, 476, 2760
Froese Fischer C., Tachiev G., 2004, Atomic Data and Nuclear Data Tables, 87, 1
Froese Fischer C., Tachiev G., Irimia A., 2006, Atomic Data and Nuclear Data Tables, 92, 607
García-Benito R., et al., 2010, MNRAS, 408, 2234
García-Burillo S., et al., 2014, A&A, 567, A125
García-Rojas J., Morisset C., Jones D., Wesson R., Boffin H. M. J., Monteiro H., Corradi R. L. M., Rodríguez-Gil P., 2022, MNRAS, 510, 5444
Garnett D. R., 1989, ApJ, 345, 282
Garnett D. R., 1992, AJ, 103, 1330
Garnett D. R., Shields G. A., Skillman E. D., Sagan S. P., Dufour R. J., 1997, ApJ, 489, 63
Goodrich R. W., Osterbrock D. E., 1983, ApJ, 269, 416
Grevesse N., Sauval A. J., 1998, Space Sci. Rev., 85, 161
Gronow S., Côté B., Lach F., Seitenzahl I. R., Collins C. E., Sim S. A., Röpke F. K., 2021, A&A, 656, A94
Groves B. A., Heckman T. M., Kauffmann G., 2006, MNRAS, 371, 1559
Guo Y., et al., 2020, ApJ, 898, 26
Guseva N. G., Izotov Y. I., Stasińska G., Fricke K. J., Henkel C., Papaderos P., 2011, A&A, 529, A149
Hägele G. F., Pérez-Montero E., Díaz Á. I., Terlevich E., Terlevich R., 2006, MNRAS, 372, 293
Hägele G. F., Díaz Á. I., Terlevich E., Terlevich R., Pérez-Montero E., Cardaci M. V., 2008, MNRAS, 383, 209
Hägele G. F., García-Benito R., Pérez-Montero E., Díaz Á. I., Cardaci M. V., Firpo V., Terlevich E., Terlevich R., 2011, MNRAS, 414, 272
Hägele G. F., Firpo V., Bosch G., Díaz Á. I., Morrell N., 2012, MNRAS, 422, 3475
Henry R. B. C., Kwitter K. B., Balick B., 2004, AJ, 127, 2284
Hummer D. G., Storey P. J., 1987, MNRAS, 224, 801
Israelian G., Rebolo R., 2001, ApJ, 557, L43

Izotov Y. I., Thuan T. X., 2008, ApJ, 687, 133

Izotov Y. I., Stasińska G., Meynet G., Guseva N. G., Thuan T. X., 2006, A&A, 448, 955

Izotov Y. I., Guseva N. G., Fricke K. J., Stasińska G., Henkel C., Papaderos P., 2010, A&A, 517, A90

Jenkins E. B., 2009, ApJ, 700, 1299

Jin Y., Kewley L. J., Sutherland R., 2022, ApJ, 927, 37

Kakkad D., et al., 2018, A&A, 618, A6

Kawasaki K., Nagao T., Toba Y., Terao K., Matsuoka K., 2017, ApJ, 842, 44

Kennicutt Robert C. J., Bresolin F., Garnett D. R., 2003, ApJ, 591, 801

Kewley L. J., Dopita M. A., Sutherland R. S., Heisler C. A., Trevena J., 2001, ApJ, 556, 121

Kewley L. J., Jansen R. A., Geller M. J., 2005, PASP, 117, 227

Kewley L. J., Nicholls D. C., Sutherland R. S., 2019, ARA&A, 57, 511

Kharb P., Lal D. V., Merritt D., 2017, Nature Astronomy, 1, 727

Kisielius R., Storey P. J., Ferland G. J., Keenan F. P., 2009, MNRAS, 397, 903

Koski A. T., 1978, ApJ, 223, 56

Kraemer S. B., Wu C.-C., Crenshaw D. M., Harrington J. P., 1994, ApJ, 435, 171

Kraemer S. B., Turner T. J., Couto J. D., Crenshaw D. M., Schmitt H. R., Revalski M., Fischer T. C., 2020, MNRAS, 493, 3893

López-Sánchez A. R., Esteban C., 2009, A&A, 508, 615

Lucertini F., Monaco L., Caffau E., Bonifacio P., Mucciarelli A., 2022, A&A, 657, A29

Luridiana V., Morisset C., Shaw R. A., 2015, A&A, 573

Maiolino R., Mannucci F., 2019, A&ARv, 27, 3

Maksym W. P., et al., 2019, ApJ, 872, 94

Malkan M. A., Oke J. B., 1983, ApJ, 265, 92

Mannucci F., et al., 2021, MNRAS, 508, 1582

Mateus A., Sodré L., Cid Fernandes R., Stasińska G., Schoenell W., Gomes J. M., 2006, MNRAS, 370, 721

Matsuoka K., Nagao T., Maiolino R., Marconi A., Taniguchi Y., 2009, A&A, 503, 721

Matsuoka K., Nagao T., Marconi A., Maiolino R., Mannucci F., Cresci G., Terao K., Ikeda H., 2018, A&A, 616, L4

Matteucci F., Padovani P., 1993, ApJ, 419, 485

Mignoli M., et al., 2019, A&A, 626, A9

Milingo J. B., Kwitter K. B., Henry R. B. C., Souza S. P., 2010, ApJ, 711, 619

Mingozzi M., et al., 2019, A&A, 622, A146

Mollá M., Díaz A. I., 2005, MNRAS, 358, 521

Monreal-Ibero A., Walsh J. R., Vílchez J. M., 2012, A&A, 544, A60

Monteiro A. F., Dors O. L., 2021, MNRAS, 508, 3023

Nagao T., Maiolino R., Marconi A., 2006, A&A, 459, 85

Nakajima K., et al., 2018, A&A, 612, A94

Nelson E. J., et al., 2012, ApJ, 747, L28

Nelson E. J., et al., 2016, ApJ, 828, 27

Nissen P. E., Chen Y. Q., Asplund M., Pettini M., 2004, A&A, 415, 993

Nissen P. E., Akerman C., Asplund M., Fabbian D., Kerber F., Kaufl H. U., Pettini M., 2007, A&A, 469, 319

Nomoto K., Kobayashi C., Tominaga N., 2013, ARA&A, 51, 457

Osterbrock D. E., 1989, Astrophysics of gaseous nebulae and active galactic nuclei

Pagel B. E. J., 1978, MNRAS, 183, 1P

Pagomenos G. J. S., Bernard-Salas J., Pottasch S. R., 2018, A&A, 615, A29

Peimbert M., Costero R., 1969, Boletin de los Observatorios Tonantzintla y Tacubaya, 5, 3

Peimbert M., Peimbert A., Delgado-Inglada G., 2017, PASP, 129, 082001

Pérez-Díaz B., Masegosa J., Márquez I., Pérez-Montero E., 2021, MNRAS, 505, 4289

Pérez-Montero E., 2017, PASP, 129, 043001

Pérez-Montero E., Contini T., 2009, MNRAS, 398, 949

Pérez-Montero E., Díaz A. I., 2003, MNRAS, 346, 105

Pérez-Montero E., Díaz A. I., Vílchez J. M., Kehrig C., 2006, A&A, 449, 193

Pérez-Montero E., et al., 2011, A&A, 532, A141

Pérez-Montero E., Dors O. L., Vílchez J. M., García-Benito R., Cardaci M. V., Hägele G. F., 2019, MNRAS, 489, 2652

Pettini M., Smith L. J., King D. L., Hunstead R. W., 1997, ApJ, 486, 665

Phillips M. M., Charles P. A., Baldwin J. A., 1983, ApJ, 266, 485

Pilyugin L. S., 2003, A&A, 399, 1003

Pilyugin L. S., Vílchez J. M., Contini T., 2004, A&A, 425, 849

Pilyugin L. S., Lara-Lopez M. A., Vilchez J. M., Duarte Puertas S., Zinchenko I. A., Dors O. L., 2022, arXiv e-prints, p. arXiv:2209.13967

Portinari L., Chiosi C., 1999, A&A, 350, 827

Prochaska J. X., Wolfe A. M., 2002, ApJ, 566, 68

Ramos Almeida C., Pérez García A. M., Acosta-Pulido J. A., Rodríguez Espinosa J. M., Barrena R., Manchado A., 2006, ApJ, 645, 148

Revalski M., Crenshaw D. M., Kraemer S. B., Fischer T. C., Schmitt H. R., Machuca C., 2018a, ApJ, 856, 46

Revalski M., et al., 2018b, ApJ, 867, 88

Revalski M., et al., 2021, ApJ, 910, 139

Revalski M., et al., 2022, ApJ, 930, 14

Richardson C. T., Allen J. T., Baldwin J. A., Hewett P. C., Ferland G. J., 2014, MNRAS, 437, 2376

Riffel R., Rodríguez-Ardila A., Pastoriza M. G., 2006, A&A, 457, 61

Riffel R. A., Storchi-Bergmann T., Zakamska N. L., Riffel R., 2020, MNRAS, 496, 4857

Riffel R. A., et al., 2021a, MNRAS, 501, L54

Riffel R., et al., 2021b, MNRAS, 501, 4064

Riffel R. A., Dors O. L., Krabbe A. C., Esteban C., 2021c, MNRAS, 506, L11

Ritter C., Herwig F., Jones S., Pignatari M., Fryer C., Hirschi R., 2018, MNRAS, 480, 538

Rodríguez-Ardila A., Prieto M. A., Portilla J. G., Tejeiro J. M., 2011, ApJ, 743, 100

Rogers N. S. J., Skillman E. D., Pogge R. W., Berg D. A., Moustakas J., Croxall K. V., Sun J., 2021, ApJ, 915, 21

Rogers N. S. J., Skillman E. D., Pogge R. W., Berg D. A., Croxall K. V., Bartlett J., Arellano-Córdova K. Z., Moustakas J., 2022, arXiv e-prints, p. arXiv:2209.03962

Roman-Duval J., et al., 2022, ApJ, 935, 105

Ruschel-Dutra D., Dall'Agnol De Oliveira B., 2020, danielrd6/ifscube v1.0, Zenodo, doi:10.5281/zenodo.3945237

Ruschel-Dutra D., et al., 2021, MNRAS, 507, 74

Samland M., Hensler G., Theis C., 1997, ApJ, 476, 544

Savage B. D., Sembach K. R., 1996, ARA&A, 34, 279

Shields G. A., Searle L., 1978, ApJ, 222, 821

Shuder J. M., 1980, ApJ, 240, 32

Shuder J. M., Osterbrock D. E., 1981, ApJ, 250, 55

Sommer-Larsen J., Götz M., Portinari L., 2003, ApJ, 596, 47

Stasińska G., 1982, A&AS, 48, 299

Stasińska G., 1984, A&A, 135, 341

Stasińska G., 1990, A&AS, 83, 501

Storchi-Bergmann T., Pastoriza M. G., 1990, PASP, 102, 1359

Storchi-Bergmann T., Schmitt H. R., Calzetti D., Kinney A. L., 1998, AJ, 115, 909

Storey P. J., Zeippen C. J., 2000, MNRAS, 312, 813

Storey P. J., Sochi T., Badnell N. R., 2014, MNRAS, 441, 3028

Takada-Hidai M., et al., 2002, ApJ, 573, 614

Tananbaum H., et al., 1979, ApJ, 234, L9

Tayal S. S., Gupta G. P., 1999, ApJ, 526, 544

Tayal S. S., Zatsarinny O., 2010, ApJS, 188, 32

Thomas A. D., et al., 2017, ApJS, 232, 11

Thomas A. D., Kewley L. J., Dopita M. A., Groves B. A., Hopkins A. M., Sutherland R. S., 2019, ApJ, 874, 100

Thuan T. X., Izotov Y. I., Lipovetsky V. A., 1995, ApJ, 445, 108

Toribio San Cipriano L., Domínguez-Guzmán G., Esteban C., García-Rojas J., Mesa-Delgado A., Bresolin F., Rodríguez M., Simón-Díaz S., 2017, MNRAS, 467, 3759

Torres-Peimbert S., Peimbert M., 1977, Rev. Mex. Astron. Astrofis., 2, 181

Vale Asari N., Stasińska G., Morisset C., Cid Fernandes R., 2016, MNRAS, 460, 1739

Vaona L., Ciroi S., Di Mille F., Cracco V., La Mura G., Rafanelli P., 2012, MNRAS, 427, 1266

Vermeij R., van der Hulst J. M., 2002, A&A, 391, 1081

Vidal-García A., Plat A., Curtis-Lake E., Feltre A., Hirschmann M., Cheval-
    lard J., Charlot S., 2022, arXiv e-prints, p. arXiv:2211.13648
Viegas-Aldrovandi S. M., Contini M., 1989, ApJ, 339, 689
Vilchez J. M., Pagel B. E. J., Diaz A. I., Terlevich E., Edmunds M. G., 1988,
    MNRAS, 235, 633
Vincenzo F., Kobayashi C., 2018, MNRAS, 478, 155
Walsh J. R., et al., 2018, A&A, 620, A169
Wiese W. L., Fuhr J. R., Deters T. M., 1996, Atomic transition probabilities
    of carbon, nitrogen, and oxygen : a critical data compilation
Woosley S. E., Weaver T. A., 1995, ApJS, 101, 181
Xu X., Arav N., Miller T., Korista K. T., Benn C., 2021, MNRAS, 506, 2725
York D. G., et al., 2000, AJ, 120, 1579
Zurita A., Bresolin F., 2012, MNRAS, 427, 1463
do Nascimento J. C., et al., 2022, MNRAS, 513, 807
van Zee L., Salzer J. J., Haynes M. P., O'Donoghue A. A., Balonek T. J.,
    1998, AJ, 116, 2805

APPENDIX A: TABLES

This paper has been typeset from a TEX/LATEX file prepared by the author.

Table A1. Emission-line intensities of Seyfert 2s relative to Hβ=1.00 taken from SDSS DR17 and compiled from the literature. For Mrk 3 the sum [S II]λ6717+6731 (in relation to Hβ) is listed. Last column lists the references for the optical and near infrared lines, except for Mrk 3 and ESO 138 G1 which the line set was taken from only one work.

Object	[O II] λ3727	[O III] λ4363	[O III] λ5007	[N II] λ5755	[S III] λ6312	Hα λ6563	[N II] λ6584	[S II] λ6716	[S II] λ6731	[S III] λ9069+λ9532	Ref.
Mrk 573	2.13 ± 0.05	0.14 ± 0.011	10.26 ± 0.05		—	2.86 ± 0.05	2.34 ± 0.04	0.79 ± 0.01	0.73 ± 0.02	2.58	1, 12[a]
NGC 5728	2.32 ± 0.03	0.11 ± 0.016	9.10 ± 0.11		—	2.86 ± 0.13	2.86 ± 0.13	0.97 ± 0.06	0.66 ± 0.03	1.92	1, 12[a]
ESO 428-G14	2.22	0.24	11.2		—	2.90	3.13	0.83	0.88	1.87	2, 12[a]
NGC 4388	2.73	0.16	10.55		—	2.84	1.50	0.72	0.62	1.10	3, 13[a]
Mrk 78	4.96	0.14	11.94		—	2.46	2.46	0.68	0.61	0.89	4, 14[a]
NGC 7674	1.29	0.12	12.55		—	3.70	3.68	0.54	0.64	3.15	5, 12[a]
NGC 2110	4.38	0.17	4.76		—	2.66	3.76	1.52	1.42	1.91	6, 12[a]
NGC 7682	2.85	0.16	9.34		—	3.10	3.03	1.09	1.17	1.95	7, 12[a]
NGC 3227	3.22	0.50	10.73		—	2.86	5.01	1.24	1.26	1.66	8, 12[b]
Mrk 1066	3.34	0.08	3.84		—	2.76	2.42	0.51	0.55	0.75	9, 12[a]
Mrk 3[b,c]	4.84	0.23	11.22		—	2.85	3.21	1.45		2.59	10
ESO 138 G1[c]	2.35 ± 0.05	0.34 ± 0.02	8.71 ± 0.25		—	3.01 ± 0.10	0.68 ± 0.03	0.47 ± 0.03	0.48 ± 0.03	0.69	11
55978-0990	6.76 ± 0.43	0.14 ± 0.06	10.70 ± 0.73		—	2.86 ± 0.31	3.30 ± 0.36	1.07 ± 0.18	0.87 ± 0.16	2.06 ± 0.66	15
56104-0966	6.31 ± 0.14	0.07 ± 0.02	8.51 ± 0.20		—	2.86 ± 0.09	1.04 ± 0.04	0.62 ± 0.03	0.56 ± 0.03	0.73 ± 0.12	15
55181-0154	4.12 ± 0.31	0.06 ± 0.03	7.82 ± 0.28		0.15 ± 0.04	2.86 ± 0.21	2.05 ± 0.15	0.60 ± 0.06	0.61 ± 0.06	2.02 ± 0.42	15
56088-0473	2.07 ± 0.01	0.06 ± 0.01	7.70 ± 0.04		0.01 ± 0.01	2.86 ± 0.01	0.15 ± 0.01	0.12 ± 0.01	0.11 ± 0.01	0.63 ± 0.02	15
56034-0154	3.02 ± 0.32	0.14 ± 0.01	11.88 ± 0.23		0.05 ± 0.03	2.86 ± 0.07	2.13 ± 0.05	0.88 ± 0.03	0.81 ± 0.03	2.10 ± 0.14	15
56067-0382	5.51 ± 1.33	0.21 ± 0.10	8.70 ± 0.83	0.192 ± 0.165	—	2.86 ± 0.52	2.36 ± 0.44	0.86 ± 0.22	0.81 ± 0.22	1.19 ± 0.89	15
56240-0340	8.32 ± 0.52	0.16 ± 0.06	7.24 ± 0.56		—	2.86 ± 0.28	2.60 ± 0.26	1.10 ± 0.21	0.86 ± 0.20	3.04 ± 0.94	15
55539-0167	2.79 ± 0.20	0.05 ± 0.02	4.11 ± 0.08	0.078 ± 0.047	—	2.86 ± 0.08	1.91 ± 0.05	0.61 ± 0.03	0.54 ± 0.03	1.08 ± 0.14	15
56626-0636	3.82 ± 0.09	0.06 ± 0.01	6.12 ± 0.10		0.10 ± 0.02	2.86 ± 0.07	2.23 ± 0.05	1.06 ± 0.03	0.98 ± 0.03	1.22 ± 0.10	15
56074-0045	4.23 ± 0.32	0.03 ± 0.01	2.69 ± 0.04		—	2.86 ± 0.07	1.52 ± 0.04	0.77 ± 0.02	0.58 ± 0.02	0.91 ± 0.11	15
55212-0380	3.52 ± 1.13	0.10 ± 0.03	12.54 ± 0.51		—	2.86 ± 0.15	2.94 ± 0.15	0.85 ± 0.06	0.84 ± 0.06	2.41 ± 0.30	15
56399-0302	5.01 ± 0.37	0.08 ± 0.04	3.07 ± 0.19		—	2.86 ± 0.23	2.16 ± 0.19	1.58 ± 0.16	1.14 ± 0.14	1.33 ± 0.63	15
56001-0293	5.05 ± 0.20	0.07 ± 0.01	7.63 ± 0.20	0.047 ± 0.037	—	2.86 ± 0.13	1.74 ± 0.08	0.85 ± 0.05	0.61 ± 0.04	1.54 ± 0.21	15
55651-0052	3.28 ± 0.76	0.02 ± 0.01	3.54 ± 0.04		0.05 ± 0.01	2.86 ± 0.06	2.06 ± 0.04	0.72 ± 0.02	0.68 ± 0.02	0.94 ± 0.08	15
56566-0794	6.58 ± 0.61	0.05 ± 0.02	4.74 ± 0.12	0.017 ± 0.016	0.08 ± 0.03	2.86 ± 0.10	2.16 ± 0.08	1.26 ± 0.06	1.07 ± 0.05	1.22 ± 0.16	15
56748-0336	4.97 ± 0.51	0.08 ± 0.05	7.11 ± 0.41		—	2.86 ± 0.24	3.23 ± 0.27	0.99 ± 0.12	0.89 ± 0.12	1.85 ± 0.50	15
56206-0454	7.35 ± 0.27	0.09 ± 0.02	6.67 ± 0.19		0.05 ± 0.03	2.86 ± 0.11	1.21 ± 0.06	1.12 ± 0.05	0.91 ± 0.05	1.08 ± 0.19	15
55860-0112	5.74 ± 1.44	0.11 ± 0.07	7.82 ± 0.66		0.15 ± 0.12	2.86 ± 0.33	5.38 ± 0.61	1.80 ± 0.23	1.77 ± 0.23	1.78 ± 0.46	15
56453-0144	3.19 ± 0.37	0.06 ± 0.02	6.42 ± 0.18		—	2.86 ± 0.10	2.64 ± 0.10	0.89 ± 0.06	0.78 ± 0.06	2.20 ± 0.31	15
55710-0116	2.72 ± 1.05	0.07 ± 0.02	7.54 ± 0.24		0.06 ± 0.04	2.86 ± 0.12	4.47 ± 0.18	1.04 ± 0.06	1.13 ± 0.07	2.58 ± 0.21	15
56209-0390	6.99 ± 0.77	0.07 ± 0.06	8.57 ± 0.97		—	2.86 ± 0.58	2.75 ± 0.55	0.39 ± 0.15	0.22 ± 0.14	0.52 ± 0.65	15
56298-0302	10.16 ± 1.84	0.09 ± 0.07	5.39 ± 0.46		—	2.86 ± 0.42	3.29 ± 0.49	1.59 ± 0.27	1.40 ± 0.24	7.00 ± 2.26	15
56366-0928	4.81 ± 0.41	0.12 ± 0.05	5.70 ± 0.40		0.21 ± 0.08	2.86 ± 0.28	2.51 ± 0.25	0.96 ± 0.12	0.96 ± 0.12	2.31 ± 0.56	15
55742-0383	2.74 ± 0.55	0.05 ± 0.01	4.99 ± 0.10	0.049 ± 0.038	—	2.86 ± 0.08	2.06 ± 0.06	0.63 ± 0.03	0.56 ± 0.03	1.01 ± 0.14	15
55302-0655	4.90 ± 0.18	0.05 ± 0.02	2.06 ± 0.05	0.035 ± 0.019	—	2.86 ± 0.08	1.67 ± 0.06	1.24 ± 0.04	1.00 ± 0.04	0.94 ± 0.14	15
56328-0550	6.45 ± 0.26	0.06 ± 0.02	4.90 ± 0.15		0.06 ± 0.04	2.86 ± 0.13	3.35 ± 0.16	1.10 ± 0.06	0.86 ± 0.06	1.57 ± 0.25	15
55646-0770	8.48 ± 2.32	0.14 ± 0.05	7.32 ± 1.31		—	2.86 ± 0.95	3.74 ± 1.23	1.50 ± 0.56	1.39 ± 0.52	1.82 ± 1.49	15
55617-0758	8.05 ± 0.33	0.05 ± 0.04	3.84 ± 0.20		0.11 ± 0.06	2.86 ± 0.27	2.26 ± 0.22	1.24 ± 0.14	1.38 ± 0.15	1.33 ± 0.40	15
56003-0218	3.35 ± 1.00	0.07 ± 0.04	4.70 ± 0.29		0.10 ± 0.07	2.86 ± 0.22	1.68 ± 0.15	0.56 ± 0.09	0.58 ± 0.09	2.06 ± 0.45	15
55629-0364	9.11 ± 0.64	0.11 ± 0.07	7.08 ± 0.52		—	2.86 ± 0.41	3.91 ± 0.57	1.44 ± 0.24	1.32 ± 0.23	1.64 ± 0.80	15
56568-0076	5.12 ± 0.59	0.03 ± 0.01	3.16 ± 0.05	0.031 ± 0.021	—	2.86 ± 0.09	2.98 ± 0.10	0.71 ± 0.03	0.69 ± 0.03	0.66 ± 0.09	15
55836-0160	3.57 ± 0.33	0.04 ± 0.02	3.70 ± 0.11		—	2.86 ± 0.14	2.24 ± 0.11	0.67 ± 0.05	0.59 ± 0.05	1.71 ± 0.32	15
55505-0654	3.05 ± 0.19	0.04 ± 0.02	7.95 ± 0.28		0.05 ± 0.03	2.86 ± 0.17	2.70 ± 0.16	0.65 ± 0.05	0.58 ± 0.05	2.10 ± 0.35	15

References— (1) Dopita et al. (2015), (2) Bergvall et al. (1986), (3) Phillips et al. (1983), (4) Koski (1978), (5) Kraemer et al. (1994), (6) Shuder (1980), (7) Thomas et al. (2017), (8) Cohen (1983), (6) Goodrich & Osterbrock (1983), (10) Malkan & Oke (1983), (11) Alloin et al. (1992). (12) Riffel et al. (2006), (13) Rodríguez-Ardila et al. (2011), (14) Ramos Almeida et al. (2006), (15) BOSS/SDSS sample, (a) Reference which the [S III]λ9069 emission line fluxes was compiled. (b) Emission-line intensities corrected by reddening in the present work. (c) Object which the [S III]λ9069 was measured with the others.

Table A2. Electron density and electron temperature values assumed in the ionic abundance calculations. $T_e(O^{2+})$ was calculated through the observational $RO3$ line ratio, whose line intensities are listed in Table A1, and by using the PyNeb code (Luridiana et al. 2015). $T_e(N^+)$ and $T_e(S^{2+})$ were calculated either from $RN2$ and $RS3$ line ratios (when these line ratios were measured), respectively, or from Eq. 3 and 4 (when auroral lines were not measured, see Table A1).

Object	$T_e(O^{2+})$ K	$T_e(S^{2+})$ K	$T_e(N^+)$ K	$N_e(\text{cm}^{-3})$
Mrk 573	12888 ± 425	21341 ± 7881	11673 ± 1899	559 ± 102
NGC 5728	12301 ± 725	20030 ± 7929	11373 ± 1923	674 ± 167
ESO 428-G14	15651 ± 1197	27501 ± 8055	13082 ± 1983	1059 ± 466
NGC 4388	13446 ± 1254	22585 ± 8074	11958 ± 1992	393:
Mrk 78	12162 ± 1139	19721 ± 8036	11303 ± 1974	475:
NGC 7674	11296 ± 1126	17790 ± 8032	10861 ± 1972	1396 ± 620
NGC 2110	20761 ± 3395	38896 ± 9338	15688 ± 2561	691 ± 300
NGC 7682	14146 ± 1412	24146 ± 8131	12315 ± 2020	1067 ± 495
NGC 3227	25028 ± 2500	48412 ± 17000	17864 ± 5800	1067 ± 485
Mrk 1066	15446 ± 3553	27045 ± 9466	12978 ± 2616	1122:
Mrk 3	15335 ± 1185	26796 ± 8051	12921 ± 1981	500:
ESO 138 G1	21996 ± 1318	41650 ± 8097	16318 ± 2003	1039 ± 452
55978-0990	12685 ± 2490	20888 ± 8684	11570 ± 2274	266:
56104-0966	10754 ± 1095	16582 ± 8023	10585 ± 1968	471 ± 210
55181-0154	10508 ± 1855	24392 ± 9679	10459 ± 2111	778 ± 384
56088-0473	10566 ± 301	9244 ± 1351	10488 ± 1893	502 ± 186
56034-0154	12184 ± 409	11052 ± 2481	11314 ± 1898	537 ± 167
56067-0382	16612 ± 5030	29644 ± 10845	31422 ± 9900	666:
56240-0340	15912 ± 3588	28083 ± 9495	13215 ± 2628	200:
55539-0167	12334 ± 1976	20105 ± 8387	16670 ± 5500	445 ± 218
56626-0636	11409 ± 726	27152 ± 5997	10919 ± 1923	537 ± 137
56074-0045	11954 ± 1531	19258 ± 8179	11197 ± 2042	127 ± 58
55212-0380	10644 ± 1185	16335 ± 8051	10528 ± 1981	699 ± 315
56399-0302	17311 ± 5347	31203 ± 11175	13929 ± 3316	50:
56001-0293	11159 ± 640	17484 ± 7913	13152 ± 4500	55:
55651-0052	9576 ± 733	18122 ± 2797	9984 ± 1923	555 ± 130
56566-0794	11713 ± 1806	21676 ± 7539	10771 ± 3800	347 ± 162
56748-0336	11981 ± 3128	19319 ± 9129	11211 ± 2471	477:
56206-0454	12842 ± 1266	16315 ± 7012	11649 ± 1994	266 ± 130
55860-0112	13038 ± 3931	27975 ± 12880	11749 ± 2753	735 ± 360
56453-0144	11224 ± 1400	17630 ± 8127	10824 ± 2017	410 ± 202
55710-0116	11189 ± 1218	10917 ± 2756	10806 ± 1986	1021 ± 381
56209-0390	10735 ± 3862	16538 ± 8150	10575 ± 2728	198 ± 49
56298-0302	14006 ± 5604	23833 ± 11451	12243 ± 3425	451 ± 215
56366-0928	15523 ± 3682	30648 ± 9727	13017 ± 2662	839 ± 410
55742-0383	11497 ± 889	18239 ± 7966	12245 ± 3500	445 ± 206
55302-0655	16672 ± 3674	29778 ± 9568	11547 ± 3178	267 ± 122
56328-0550	12373 ± 1714	14346 ± 5621	11410 ± 2080	192:
55646-0770	14856 ± 3805	25729 ± 9680	12676 ± 2706	593:
55617-0758	12640 ± 4540	27347 ± 10109	11546 ± 2987	1168 ± 560
56003-0218	13337 ± 3563	16884 ± 8330	11902 ± 2620	913 ± 430
55629-0364	13575 ± 4192	22872 ± 10028	12023 ± 2852	546:
56568-0076	11281 ± 1368	17756 ± 8115	10853 ± 2012	666 ± 215
55836-0160	11814 ± 2314	18946 ± 8576	11125 ± 2225	427 ± 205
55505-0654	9268 ± 1446	11052 ± 2955	9827 ± 2026	422 ± 190

Note. For some objects we use ":" to indicate that error bars are at least an order of magnitude larger than the expected density. This is due to the significant emission-line errors (see Sect 3.1).

Table A3. Ionic and total abundances for Seyfert 2 nuclei derived through the T_e-method.

Object	O^+/H^+	O^{2+}/H^+	O/H	S^+/H^+	S^{2+}/H^+	ICF(S)	S/H	S/O
Mrk 573	7.95 ± 0.12	8.21 ± 0.04	8.58 ± 0.13	6.46 ± 0.12	6.52 ± 0.16	2.02	7.08 ± 0.18	-1.50 ± 0.22
NGC 5728	8.03 ± 0.12	8.22 ± 0.07	8.61 ± 0.14	6.52 ± 0.12	6.42 ± 0.17	1.81	7.07 ± 0.18	-1.55 ± 0.23
ESO 428-G14	7.79 ± 0.10	8.03 ± 0.07	8.40 ± 0.12	6.44 ± 0.10	6.24 ± 0.15	1.95	6.94 ± 0.16	-1.46 ± 0.20
NGC 4388	8.03 ± 0.12	8.17 ± 0.09	8.59 ± 0.13	6.37 ± 0.12	6.12 ± 0.16	1.83	6.85 ± 0.18	-1.74 ± 0.22
Mrk 78	8.38 ± 0.13	8.35 ± 0.10	8.84 ± 0.14	6.41 ± 0.13	6.10 ± 0.17	1.52	6.87 ± 0.19	-1.97 ± 0.23
NGC 7674	7.85 ± 0.13	8.47 ± 0.10	8.74 ± 0.15	6.47 ± 0.13	6.71 ± 0.18	2.94	7.20 ± 0.19	-1.54 ± 0.24
NGC 2110	7.84 ± 0.10	7.39 ± 0.09	8.15 ± 0.11	6.50 ± 0.10	6.30 ± 0.14	1.22	6.71 ± 0.16	-1.43 ± 0.19
NGC 7682	7.99 ± 0.12	8.06 ± 0.09	8.50 ± 0.13	6.61 ± 0.11	6.33 ± 0.16	1.61	7.08 ± 0.17	-1.42 ± 0.22
NGC 3227	7.55 ± 0.14	7.59 ± 0.06	8.04 ± 0.15	6.36 ± 0.15	6.28 ± 0.19	1.72	6.62 ± 0.21	-1.42 ± 0.26
Mrk 1066	7.98 ± 0.13	7.58 ± 0.11	8.30 ± 0.14	6.24 ± 0.13	5.85 ± 0.17	1.21	6.68 ± 0.19	-1.62 ± 0.24
Mrk 3	8.16 ± 0.11	8.05 ± 0.07	8.58 ± 0.12	6.62 ± 0.11	6.40 ± 0.15	1.46	7.11 ± 0.17	-1.47 ± 0.21
ESO 138 G1	7.52 ± 0.08	7.60 ± 0.05	8.04 ± 0.09	6.00 ± 0.08	5.78 ± 0.12	1.74	6.20 ± 0.14	-1.83 ± 0.16
55978-0990	8.49 ± 0.14	8.25 ± 0.09	8.86 ± 0.15	6.55 ± 0.14	6.43 ± 0.18	1.35	7.09 ± 0.20	-1.78 ± 0.25
56104-0966	8.60 ± 0.14	8.37 ± 0.11	8.97 ± 0.15	6.44 ± 0.14	6.12 ± 0.18	1.32	6.90 ± 0.20	-2.08 ± 0.25
55181-0154	8.42 ± 0.15	8.36 ± 0.11	8.87 ± 0.16	6.48 ± 0.15	6.34 ± 0.19	1.43	7.01 ± 0.21	-1.86 ± 0.26
56088-0473	8.13 ± 0.14	8.35 ± 0.04	8.73 ± 0.15	5.74 ± 0.14	6.50 ± 0.18	1.89	6.86 ± 0.20	-1.87 ± 0.25
56034-0154	8.16 ± 0.12	8.35 ± 0.04	8.74 ± 0.14	6.53 ± 0.12	6.87 ± 0.17	1.87	7.32 ± 0.18	-1.41 ± 0.23
56067-0382	7.58 ± 0.16	7.86 ± 0.13	8.04 ± 0.17	6.03 ± 0.15	6.01 ± 0.19	1.31	6.32 ± 0.21	-1.72 ± 0.27
56240-0340	8.38 ± 0.13	7.82 ± 0.10	8.66 ± 0.14	6.43 ± 0.13	6.44 ± 0.17	1.18	7.03 ± 0.19	-1.63 ± 0.23
55539-0167	7.58 ± 0.15	7.87 ± 0.10	8.22 ± 0.16	6.03 ± 0.15	6.17 ± 0.20	1.32	6.70 ± 0.22	-1.53 ± 0.27
56626-0636	8.32 ± 0.13	8.14 ± 0.07	8.72 ± 0.14	6.65 ± 0.13	6.06 ± 0.17	1.35	7.04 ± 0.19	-1.68 ± 0.24
56074-0045	8.35 ± 0.13	7.73 ± 0.09	8.62 ± 0.14	6.41 ± 0.13	6.12 ± 0.17	1.15	6.88 ± 0.19	-1.74 ± 0.24
55212-0380	8.34 ± 0.14	8.55 ± 0.10	8.94 ± 0.15	6.62 ± 0.14	6.65 ± 0.18	1.81	7.22 ± 0.20	-1.71 ± 0.25
56399-0302	8.10 ± 0.14	7.37 ± 0.12	8.35 ± 0.15	6.51 ± 0.14	6.47 ± 0.18	1.13	6.79 ± 0.20	-1.56 ± 0.25
56001-0293	8.19 ± 0.17	8.27 ± 0.07	8.71 ± 0.18	6.29 ± 0.15	6.41 ± 0.19	1.38	6.95 ± 0.21	-1.76 ± 0.28
55651-0052	8.41 ± 0.15	8.16 ± 0.10	8.78 ± 0.16	6.58 ± 0.15	6.17 ± 0.19	1.28	7.01 ± 0.21	-1.77 ± 0.26
56566-0794	8.57 ± 0.13	8.00 ± 0.11	8.85 ± 0.14	7.06 ± 0.16	6.18 ± 0.20	1.16	7.40 ± 0.22	-1.45 ± 0.26
56748-0336	8.39 ± 0.15	8.14 ± 0.12	8.76 ± 0.16	6.58 ± 0.15	6.43 ± 0.19	1.32	7.10 ± 0.21	-1.66 ± 0.26
56206-0454	8.51 ± 0.12	8.03 ± 0.10	8.81 ± 0.14	6.56 ± 0.12	6.30 ± 0.17	1.20	7.04 ± 0.18	-1.77 ± 0.23
55860-0112	8.37 ± 0.15	8.08 ± 0.12	8.72 ± 0.16	6.83 ± 0.15	6.21 ± 0.19	1.27	7.22 ± 0.21	-1.51 ± 0.27
56453-0144	8.26 ± 0.14	8.19 ± 0.09	8.70 ± 0.15	6.56 ± 0.14	6.56 ± 0.18	1.47	7.15 ± 0.20	-1.55 ± 0.25
55710-0116	8.18 ± 0.13	8.26 ± 0.11	8.70 ± 0.15	6.72 ± 0.13	6.97 ± 0.18	1.58	7.45 ± 0.20	-1.25 ± 0.24
56209-0390	8.66 ± 0.17	8.38 ± 0.13	9.02 ± 0.18	6.12 ± 0.14	5.97 ± 0.19	1.32	6.65 ± 0.20	-2.37 ± 0.27
56298-0302	8.56 ± 0.16	7.83 ± 0.13	8.81 ± 0.17	6.70 ± 0.15	6.89 ± 0.19	1.10	7.40 ± 0.21	-1.42 ± 0.27
56366-0928	8.13 ± 0.13	7.74 ± 0.11	8.46 ± 0.14	6.48 ± 0.13	6.81 ± 0.17	1.22	6.98 ± 0.19	-1.48 ± 0.24
55742-0383	7.99 ± 0.16	8.04 ± 0.09	8.50 ± 0.17	6.30 ± 0.15	6.20 ± 0.20	1.41	6.84 ± 0.21	-1.65 ± 0.28
55302-0655	8.35 ± 0.16	7.23 ± 0.11	8.56 ± 0.18	6.61 ± 0.15	5.91 ± 0.20	1.09	6.98 ± 0.21	-1.58 ± 0.28
56328-0550	8.50 ± 0.13	7.94 ± 0.11	8.78 ± 0.14	6.56 ± 0.13	6.55 ± 0.17	1.17	7.15 ± 0.19	-1.63 ± 0.24
55646-0770	8.42 ± 0.13	7.90 ± 0.11	8.71 ± 0.15	6.66 ± 0.14	6.26 ± 0.18	1.17	7.10 ± 0.20	-1.62 ± 0.25
55617-0758	8.54 ± 0.16	7.81 ± 0.12	8.79 ± 0.17	6.74 ± 0.16	6.10 ± 0.21	1.09	7.12 ± 0.22	-1.67 ± 0.28
56003-0218	8.11 ± 0.14	7.83 ± 0.11	8.47 ± 0.15	6.34 ± 0.14	6.56 ± 0.19	1.27	7.05 ± 0.20	-1.42 ± 0.26
55629-0364	8.54 ± 0.15	7.99 ± 0.12	8.82 ± 0.16	6.69 ± 0.15	6.28 ± 0.19	1.16	7.12 ± 0.21	-1.70 ± 0.26
56568-0076	8.45 ± 0.14	7.87 ± 0.10	8.73 ± 0.15	6.50 ± 0.13	6.03 ± 0.18	1.13	6.92 ± 0.20	-1.81 ± 0.25
55836-0160	8.26 ± 0.14	7.88 ± 0.11	8.59 ± 0.15	6.41 ± 0.14	6.41 ± 0.18	1.23	7.00 ± 0.20	-1.59 ± 0.25
55505-0654	8.42 ± 0.15	8.56 ± 0.11	8.97 ± 0.17	6.53 ± 0.16	6.87 ± 0.20	1.74	7.33 ± 0.22	-1.65 ± 0.27